

Utah State University

DigitalCommons@USU

All Graduate Plan B and other Reports


Graduate Studies

5-2023

An Integrated Experimental and Modeling Approach to Design Rotating Algae Biofilm Reactors (RABRs) Via Optimizing Algae Biofilm Productivity, Nutrient Recovery, and Energy Efficiency

Gerald Benjamin Jones
Utah State University

Follow this and additional works at: <https://digitalcommons.usu.edu/gradreports>

 Part of the [Biological Engineering Commons](#), [Ordinary Differential Equations and Applied Dynamics Commons](#), and the [Partial Differential Equations Commons](#)

Recommended Citation

Jones, Gerald Benjamin, "An Integrated Experimental and Modeling Approach to Design Rotating Algae Biofilm Reactors (RABRs) Via Optimizing Algae Biofilm Productivity, Nutrient Recovery, and Energy Efficiency" (2023). *All Graduate Plan B and other Reports*. 1719.

<https://digitalcommons.usu.edu/gradreports/1719>

This Report is brought to you for free and open access by the Graduate Studies at DigitalCommons@USU. It has been accepted for inclusion in All Graduate Plan B and other Reports by an authorized administrator of DigitalCommons@USU. For more information, please contact digitalcommons@usu.edu.



AN INTEGRATED EXPERIMENTAL AND MODELING APPROACH TO DESIGN
ROTATING ALGAE BIOFILM REACTORS (RABRS) VIA OPTIMIZING ALGAE BIOFILM
PRODUCTIVITY, NUTRIENT RECOVERY, AND ENERGY EFFICIENCY

by

Gerald B. Jones

A thesis submitted in partial fulfillment
of the requirements for the degree

of

MASTERS OF SCIENCE

in

Mathematics

Approved:

Dr. Jia Zhao
Major Professor

Dr. Ronald Sims
Committee Member

Dr. Luis Gordillo
Committee Member

Richard Cutler
Vice Provost of Graduate Studies

UTAH STATE UNIVERSITY
Logan, Utah

2023

Copyright © Gerald B. Jones, 2023

All Rights Reserved

ABSTRACT

Microalgae biofilms have been demonstrated to recover nutrients from wastewater and serve as biomass feedstock for bioproducts. However, there is a need to develop a platform to quantitatively describe microalgae biofilm production, which can provide guidance and insights for improving biomass areal productivity and nutrient uptake efficiency. This paper proposes a unified experimental and theoretical framework to investigate algae biofilm growth on a rotating algae biofilm reactor (RABR). The experimental laboratory setups are used to conduct controlled experiments on testing environmental and operational factors for RABRs. We propose a differential-integral equation-based mathematical model for microalgae biofilm cultivation guided by laboratory experimental findings. The predictive mathematical model development is coordinated with laboratory experiments of biofilm areal productivity associated with ammonia and inorganic phosphorus uptake by RABRs. The unified experimental and theoretical tool is used to investigate the effects of RABR rotating velocity, duty cycle, and light intensity on algae biofilm growth, areal productivity, nutrient uptake efficiency, and energy efficiency in wastewater treatment. Our framework indicates that maintaining a reasonable light intensity range results in better biomass areal productivity and nutrient uptake efficiency. Our framework also indicates that faster RABR rotation benefits biomass areal productivity. However, maximizing the nutrient uptake efficiency requires a reasonably low RABR rotating speed. Meanwhile, energy efficiency is strongly correlated with RABR rotating speed and duty cycle. Following these developments, we then extend our model to become a partial differential equation (PDE) based model that takes into consideration the spatial heterogeneity present in the reactor, by incorporating the spatial resolution of the substratum on which the algae biofilm grows within the RABR. In the proposed model extension, we conduct an extensive series of numerical simulations to better understand algae biofilm growth in an outdoor setting. Our primary focus in these simulations is to investigate the impact of various harvesting strategies and frequencies on the overall biomass productivity of the algae biofilm. Our model and numerical results provide valuable insights into optimizing algae biofilm growth and harvesting techniques in RABR systems in the context of a heterogeneous system.

PUBLIC ABSTRACT

Microalgae biofilms can grow on a rotating algae biofilm reactor (RABR) as a way to clean wastewater and provide a source of biomass for creating valuable products. However, we need a quantitative way to understand how these algae biofilms grow to make the RABR more efficient and productive. In this study, we designed experiments in the lab to test different factors that might affect the growth of the biofilms, such as how fast the RABR spins and how much light it gets. We then used these results as guidance to create a mathematical model that helps us predict how microalgae biofilms will grow in different situations. Our new method allows us to test various conditions for growing these biofilms so they can clean wastewater more effectively and provide more biomass simultaneously. Additionally, we have investigated the energy efficiency of the process, which is closely tied to the speed of the RABR and how often it rotates. By understanding these factors, we can develop better ways to use microalgae biofilms for cleaning wastewater and producing valuable biomass.

ACKNOWLEDGMENTS

I first would like to thank my major professor, Dr. Jia Zhao, for his mentorship throughout my research career at Utah State University. Dr. Zhao has been a supportive and consistent mentor and I am grateful to him for introducing me to academic research. I and Jia Zhao would like to acknowledge the support from the National Science Foundation (NSF) USA with DMS-1816783 for their assistance in funding this research.

I would like to also thank my mentor within the industry, Dr. Ronald Sims. Through his guidance and encouragement, I have been able to immerse myself in the world of biological engineering and become involved with laboratory research and industry as part of my academic career. Without either of these people, my career in research at Utah State would not have been near as accomplished nor as fun. Ronald Sims would like to acknowledge that research has been sponsored, in part, by the U.S. Department of Energy EERE - Bioenergy Technologies Office (BETO) Award EE0009271 to Utah State University titled 'Synergistic Municipal Wastewater Treatment Using a Rotating Algae Biofilm Reactor'.

I would like to acknowledge members of the Sustainable Waste-to-Bioproduct Engineering Center (SWBEC) for their collaboration and assistance in the construction and data collection of rotating algae biofilm reactors (RABRs) of many shapes and sizes. I have been fortunate to work with these talented colleagues and have been able to call many of them my friends.

Lastly, I would like to thank my parents, Gerald and Stephanie Jones. Ever since I began my schooling over twenty years ago, they have been supportive of my academic endeavors and have helped me foster my passions in mathematics and computer science.

Gerald B. Jones

CONTENTS

ABSTRACT	iii
PUBLIC ABSTRACT	iv
ACKNOWLEDGMENTS	v
LIST OF TABLES	viii
LIST OF FIGURES	ix
CHAPTER	
1. Introduction	1
2. Experimental and Theoretical Investigations of Rotating Algae Biofilm Reactors (RABRs): Areal Productivity, Nutrient Recovery, and Energy Efficiency	5
2.1 Materials and Methods	5
2.1.1 Laboratory rationale and setups	5
2.1.2 Mathematical model formulation	8
2.2 Results	12
2.3 Discussion	21
3. Exploring Microalgae Growth in Heterogeneous Rotating Algal Biofilm Reactors (RABR) through Computational Modeling	26
3.1 Mathematical Model Formulation	26
3.1.1 Photosynthetic kinetics with spatial heterogeneity	27
3.1.2 Light mechanism	28
3.1.3 Nutrient uptake mechanism	29
3.1.4 Water evaporation mechanism	30
3.1.5 Biofilm thickness	30
3.1.6 Governing equations	32
3.1.7 Harvesting mechanism	33
3.1.8 Numerical methods	35
3.2 Results	36
4. Conclusion	42
REFERENCES	44
APPENDICES	49
A. Supplemental materials for Chapter 2	49
A.1 AI procedure/method summary	49
A.2 Bomb calorimeter procedure/method summary	49
A.3 Defining total power within simulations	50
A.4 Governing equations	51

A.5	Parameters	51
A.6	Parameter tuning	52
A.7	Numerical methods	53
A.8	Supplemental figures	54

LIST OF TABLES

Table	Page
2.1 Autotrophic Index values for biofilm samples in different duty cycles.	13
2.2 Microscopic characterization of algae biofilm. This table summaries the identified algae and Cyanobacteria.	13
2.3 Areal energy content of biofilm microalgae (kJ/m^2)	13
3.1 Parameter table with fixed parameter values.	32
3.2 Parameter table with experimental parameter values.	33
3.3 Parameter table with undetermined parameter values.	33
3.4 Final productivity values of selected harvest strategies.	39
3.5 Final productivity values of selected harvest frequencies.	41
A.1 Parameter table with fixed parameter values.	51
A.2 Parameter table with experimental parameter values.	52
A.3 Parameter table with tuned parameter values.	52

LIST OF FIGURES

Figure	Page
1.1 A side view of the pilot scale RABR operating at the Central Valley Water Reclamation Facility (CVWRF). The algae biofilm is grown on a square substratum sheet and rotated into a 4,500 L tank containing anaerobic digester effluent. A plastic polycarbonate cover has been mounted to reduce heat loss in the winter months.	2
2.1 This figure provides an overview of the laboratory experiment setups for RABRs using 1 L of anaerobic digester effluent. Initially, the nine RABRs were constructed using wooden boxes lined with plastic with a photosynthetic photon flux density (PPFD) of $700\mu\text{mol}/(\text{m}^2\text{s})$, as illustrated in (a). Later on, the RABRs were transferred into plastic containers, as depicted in (b), with a higher PPFD of $1000\mu\text{mol}/(\text{m}^2\text{s})$	6
2.2 This figure shows a side view (a), and an aerial view (b) of some of the rotating algae biofilm reactors (RABRs) used to obtain empirical data on algae biomass growth. Four RABRs were placed within two 40L tanks containing anaerobic digester effluent. Three sections across RABRs were sampled daily over 11 days. A section was delineated by the black zip ties.	8
2.3 This figure depicts a schematic illustration of the rotating algal biofilm reactors (RABRs) and the photosynthetic system. The left panel shows a computational model proposed for RABRs, while the right panel illustrates the reactive kinetics taken from [40].	9
2.4 This figure shows the areal productivity of the four rotating algae biofilm reactors (RABRs) over an 11-day experiment, measured in units of $\text{g}/(\text{m}^2\text{d})$. The experiment involved a change in anaerobic digester effluent on day 6. The confidence intervals (95%) were constructed using the triplicate measurements obtained on each day. A parameter study on the growth rate k indicated that $k = 5 \times 10^{-5}$	14
2.5 A timeline of the ammonia effluent levels throughout the experiment. Black dotted lines correspond to a replacement of anaerobic digester effluent, and the red line corresponds to the parameter change of $700\mu\text{mol}/(\text{m}^2\text{s})$ to $1000\mu\text{mol}/(\text{m}^2\text{s})$	14
2.6 This figure shows the total nutrient depletion over time for ammonia (a) and phosphorus (b). Parameter fittings for the total nutrient depletion rate γ_T indicates that $\gamma_T = 8.47 \times 10^9 \text{d}^{-1}$ for ammonia, and $\gamma_T = 1.764 \times 10^{10} \text{d}^{-1}$ for phosphorus.	15
2.7 This figure displays the growth of algae biofilm over time under varying peripheral velocity (RPM) and photosynthetic photon flux density (PPFD) conditions. The algae biofilm heights over time at $t = 12, 23, 36,$ and 48 hours are shown.	16
2.8 This figure presents snapshots of algae biofilm areal productivity at 12-hour intervals over time. It shows the effects of varying peripheral velocity (RPM) and photosynthetic photon flux density (PPFD) on algae biofilm areal productivity through a parameter study.	17
2.9 This figure illustrates the changes in nutrient concentration over time under different peripheral velocities (RPM) and photosynthetic photon flux density (PPFD) conditions, as determined by a parameter study.	18

2.10	This figure shows the energy efficiency plotted against duty cycle and velocity, with a duty cycle period of 60 seconds, utilizing parameters provided in the tables.	19
2.11	This figure shows the energy efficiency at various operational settings. Here we fixed duty cycle period as 60 seconds and use the same parameters provided in the tables.	20
2.12	This figure shows the energy efficiency under various duty cycle periods. All the parameters are the same as in the previous study except for the duty cycle period.	21
3.1	A schematic illustration of the rotating algal biofilm reactors (RABR) and the photosynthetic system. This figure illustrates the proposed computational model for the rotating algal biofilm reactor (RABR) on the left.	27
3.2	Light intensity over time. The figure illustrates 24-hour PAR data as red points, with a fitted continuous function represented by a blue curve. This continuous function will be employed for subsequent simulations, starting at $t = 8$ hours for the interpolated function within the model for simulations.	29
3.3	A schematic illustration of the harvesting strategies explored within this paper. The areas shaded in red represent the mass that will be removed following the corresponding harvest strategy. The minimum height that will be considered for removal during a harvest is set with h_{harvest} .	35
3.4	This figure displays the biofilm height along the spatial variable x over a seven-day simulation within a nutrient-limited system. At Day 6, E_T approaches 0 and stalls biofilm growth.	37
3.5	This figure displays the biofilm height along the spatial variable x over a seven-day simulation in which $v = 0$ between days 3 and 4. The lack of spinning creates a heterogeneous biofilm and recovers into a more homogeneous structure after day 4.	38
3.6	This figure displays the biofilm height along the spatial variable x over a four-day simulation. The biofilm resides in a nutrient-rich system, and no harvesting occurs. This is shown as a control compared to the results in Figure 3.7.	38
3.7	This figure compares four harvesting strategies for a RABR over four-day simulations. At $t = 2$ days, a harvest is performed in each simulation. A different harvesting strategy is used in each subfigure in which $h_{\text{harvest}} = 0.0005$. See Methods for details on each harvesting strategy.	39
3.8	This figure presents a comparison of four harvesting frequencies in a RABR over a series of fourteen-day simulations. In each subfigure, the checker harvest strategy is employed, with $h_{\text{harvest}} = 0.0005$. For further details on each harvesting strategy, refer to the previous section.	41
A.1	Ammonia data from Figure 2.5 grouped by their relative time since the most recent influent replacement. Figure (a) visualizes the data for all sampling with $700\mu\text{mol}/(\text{m}^2\text{s})$, and (b) shows the data with $1000\mu\text{mol}/(\text{m}^2\text{s})$. The concentration is measured by mg/L .	54
A.2	All phosphorus data grouped by epochs of influent replacement. The red dot is the average for that day, and the blue lines are the 95% confidence intervals. The concentration is measured by mg/L .	54
A.3	The average value of the activated state (B state) of all algae biofilm layers over time, measured every minute, and a total time of 3 days. In (a), we use 375 RPM, and in (b), we use 0.0375 RPM. The gaps of time in which the activated state (B) equals $= 0$ correspond to when $\text{PPFD} = 0\mu\text{mol}/(\text{m}^2\text{s})$ to mimic the diurnal cycle described in Section 2. The parameters used to produce these figures are taken from the parameter tables A.1, A.2 and A.3.	55

A.4	The value of $(E(t) - E_T(t))$ over time, measured every 60 seconds and a total time of 3 days. In (a), we use 375 RPM, and in (b) we use 0.0375 RPM. The gaps of time in which $E - E_T = 0$ correspond to when $PPFD = 0 \mu\text{mol}/(\text{m}^2\text{s})$ to mimic the diurnal cycle described in Section 2. The rest parameters used to produce these results are taken from parameters tables A.1, A.2 and A.3.	55
A.5	This figure displays the values of A, B, and C for all 10 layers in a simulation of 30 minutes with $p = 10$. All parameters used in the simulation are the same as those used to generate the surface plots presented in Section 3, with the exception of the PPFD, which was held constant at 700, and a RABR peripheral velocity of 1 RPM.	56
A.6	This figure illustrates a parameter study of the number of layers in the numerical scheme, using the same parameters as those selected in Figure 2.6, with the exception of the PPFD, which was held constant at 700, and a RABR peripheral velocity of 1 RPM. Panel (a) shows the results at 8 hours, panel (b) at 1 day, and panel (c) at 72 hours. As the number of discretized layers in the numerical scheme decreases, the biofilm height is underestimated.	57
A.7	This figure displays the contour plots to supplement the results in Figure 2.7. . .	58
A.8	This figure displays the contour plots to supplement the results in Figure 2.8. . .	59
A.9	This figure displays the contour plots to supplement the results in Figure 2.9. . .	60

CHAPTER 1

INTRODUCTION

Microalgal biofilms, which are often attached to a surface in aquatic environments, comprise a synergistic consortium of microalgae and other microorganisms embedded within extracellular polymeric substances (EPS). Microalgal biofilms are often found on human-made structures such as drainage pipes, building walls, ship bodies, and swimming pools [37]. Microalgal biofilms have recently attracted considerable interest worldwide because of their excellent promise for biotechnological applications, including wastewater treatment and bioremediation, and for adverse effects due to biofouling. Due to their renewable, sustainable, and economical properties, they are also resources for biofuels, biopolymers, bioactive metabolites, bioactive medicinal products, and food ingredients [34, 1, 35, 42, 27, 26]. Thus, microalgal biofilms have great potential to support the building of a bio-based economy. They can contribute new solutions to some of the grand challenges of the 21st century.

Rotating algae biofilm reactors (RABRs) have been used to combine nutrient recovery from wastewater through uptake by attached-growth microalgal biofilms with harvesting by physical scraping from a growth surface. RABR biofilms cultivated on municipal and industrial wastewaters have been demonstrated to serve as feedstocks for microbial and chemical transformations to value bioproducts that include biofuels, biofertilizers, bioplastics, and chemicals for improved animal gut health and plant growth [9, 39]. Engineering challenges related to algae-based biofilm reactors for these dual applications have been reviewed and addressed [10, 23, 2]. RABR and rotating algae bioreactors (RAB) systems are relatively new compared with traditional suspended culture open raceway pond (ORP) systems and were recently compared by [28]. Several other studies [17, 24, 25] compared ORP and RAB cultures systems, demonstrating the benefits in terms of biomass productivities, achieving productivities up to 700% higher in RAB than ORP, under the same geographical and meteorological conditions [25].

Difficulties in cultivating, harvesting, concentrating, and dewatering algae-based biomass grown in suspended cultures have limited the development of an effective biomass production pro-



Figure 1.1: A side view of the pilot scale RABR operating at the Central Valley Water Reclamation Facility (CVWRF). The algae biofilm is grown on a square substratum sheet and rotated into a 4,500 L tank containing anaerobic digester effluent. A plastic polycarbonate cover has been mounted to reduce heat loss in the winter months.

cess. Initiated in 2012 by the Sustainable Waste-to-Bioproducts Engineering Center [10], The RABR consists of a rotating growth surface partially submerged in wastewater. The rotation alternately exposes the growth surface with naturally occurring microalgae and heterotrophic bacteria to the wastewater to contact nutrients and microbially produced carbon dioxide and to the atmosphere for sunlight energy and atmospheric carbon dioxide. No additional light energy or carbon dioxide addition is necessary for effective operation. The RABR was the first engineered algae biofilm reactor designed and operated outdoors open to the environment to treat wastewater from municipal and industrial operations to remove nutrients, including phosphorus and nitrogen, and to utilize the harvested algae biofilm to produce bioproducts. RABR bioproducts that have been produced include bioplastic [32], phycocyanin [38], struvite biofertilizer [20], biodiesel [5], biocrude [36], and dietary protein in lactation dairy diets [41]. The RABR operates without the need for a separate process to separate algae from water but combines both upstream biomass production with downstream microalgae separation from water through simple physical scraping. The RABR also has achieved a solids content of 12-16% solids by controlling the rotation rate of the growth platform and has been utilized in water with high turbidity, and color [41, 36]. A pilot scale (4,500 L) RABR operating at the Central Valley Water Reclamation Facility (CVWRF) for nutrient removal and for biomass feedstock for biofuel, bioplastic, and biofertilizer production is shown in Figure 1.1 and represents a physical model of a microalgae-based biofilm reactor for wastewater reclamation.

This paper aims to address the need for a quantitative understanding of algae-based biomass productivity, nutrient uptake, and energy efficiency on the RABRs under various environmental

factors and operational parameters. When disregarding other confounding factors, the primary mechanisms for algae biomass accumulation in algae are photosynthesis and endogenous respiration. While other variables such as temperature and pH can be used to predict biofilm growth, one critical environmental factor is the light intensity, which is measured as photosynthetic photon flux density (PPFD) with units of μmol of photons per square meter per second, i.e., $\mu\text{mol}/(\text{m}^2\text{s})$. Critical operational parameters include the duty cycle (the ratio of the cycling time over the total time), RABR rotating speed, hydraulic retention time and harvesting strategy. Fine-tuning the RABR through experiments to boost algae biomass productivity and nutrient consumption is both time and cost-prohibitive, making theoretical predictions with data-driven mathematical models a promising option.

Here we briefly point out some seminal works on model developments. Mathematical models focusing on PPFD as a predictor for biofilm growth have three light regimes to consider: (1) light-dependent photosynthesis, (2) light saturation of photosynthesis, and (3) light toxicity to photosynthesis. At lower light intensities, the rate of photosynthesis is directly proportional to incident light. The incident light limits the rate of photosynthesis. The biofilm becomes 'light-saturated' at a certain threshold and is not limited by incident light but by the photosystem's photosynthesis rate. At higher light intensities, the biofilm exhibits photoinhibition, and the rate of photosynthesis decreases as light intensity increases. There are two major classes of mathematical models with PPFD. The first class of models developed were macroscale models. When constructing a macroscale model, the underlying assumption is that the photosynthesis of the entire culture is a function of the average incident light reaching a culture. Some examples of this relationship include a hyperbolic tangent model, a Poisson model, and a Monod-like relationship model [8, 13, 11]. The other primary classification of models is photosystem models. In contrast to macroscale models, photosystem models takes the non-uniform incident light of culture into account. They consider both the impacts of light gradients and short light cycles. Using Beer Lambert's law of light attenuation, photosystem models employ a functional relationship between the depth of the algae biofilm and its PPFD [15]. A systematical review paper on modeling the effects of light and temperature on algae growth can be found in [6]. Extending the photosystem model to rotating algae biofilm reactors has been the focus of several studies. For example, in [4], the authors investigated the impact of sunlight intensity and exposure on the productivity of the biofilm in Rotating Algae Biofilm (RAB). A spatial model that describes the growth dynamics of a photosynthetic algae biofilm was developed in [31], while a time-space model for algae biofilm growth for biofuel production was proposed in [30]. To optimize and control the RABR, parameter studies of rotation velocity and its effect on productivity have

been conducted, and harvesting strategies, such as the frequency and proportion of harvesting, have been modeled to optimize productivity [22, 31]. Furthermore, multivariate parameter studies have been conducted to determine optimal biofilm growth, considering light intensity, the substratum exposure fraction to the atmosphere, and RABR peripheral velocity [22].

However, most of the existing mathematical models are phenomenological, and there is no experimental justification, making their predictions less convincing. This paper aims to bridge this gap between experimental data and theoretical models, making the mathematical models closer to reality and providing convincing predictions on better design of the RABR to maximize algae-based biomass productivity and nutrient uptake while maintaining low energy cost. The experimental and theoretical results will serve as a guide to achieving better practical RABRs, operation settings, and performance to treat anaerobic digester effluent using trickling filter algae as inoculum. Additionally, the results in this paper are useful for predicting the outcomes of certain scenarios in industrial settings that are not trivial to test experimentally due to cost and time constraints.

CHAPTER 2
EXPERIMENTAL AND THEORETICAL INVESTIGATIONS OF ROTATING ALGAE
BIOFILM REACTORS (RABRS): AREAL PRODUCTIVITY, NUTRIENT RECOVERY, AND
ENERGY EFFICIENCY

2.1 Materials and Methods

2.1.1 Laboratory rationale and setups

Though the RABR has been utilized on both pilot and industrial scales, controlled laboratory experiments are more effective for data collection from both time and cost perspectives. These laboratory findings will meanwhile help provide insights and guidance. The laboratory RABR experiments are easy to conduct and provide an alternative way to investigate the algae biomass areal productivity and nutrient uptake efficiency.

Three sets of triplicate RABRs (nine in total) with a volume of 1L each and plan view area of 77.01cm^2 and 4-ply cotton substratum surface area of 175 cm^2 were utilized to test the effects of light intensity, measured as photosynthetic photon flux density (PPFD) and the duty cycle, which may occur during the night when there is no photosynthesis occurring. The RABR setups are shown in Figure 2.1. PPFD values were selected to represent mid-summer ($1000\text{ }\mu\text{mol}/(\text{m}^2\text{s})$) and mid-autumn ($700\text{ }\mu\text{mol}/(\text{m}^2\text{s})$) in Northern Utah using light-emitting diodes. To mimic the diurnal cycle, the incident light is set to “on” for 14 hours and then “off” for 10 hours for one day. Nutrient uptake for each PPFD value was tested for five weeks, to a total testing duration of ten weeks for both PPFD values.

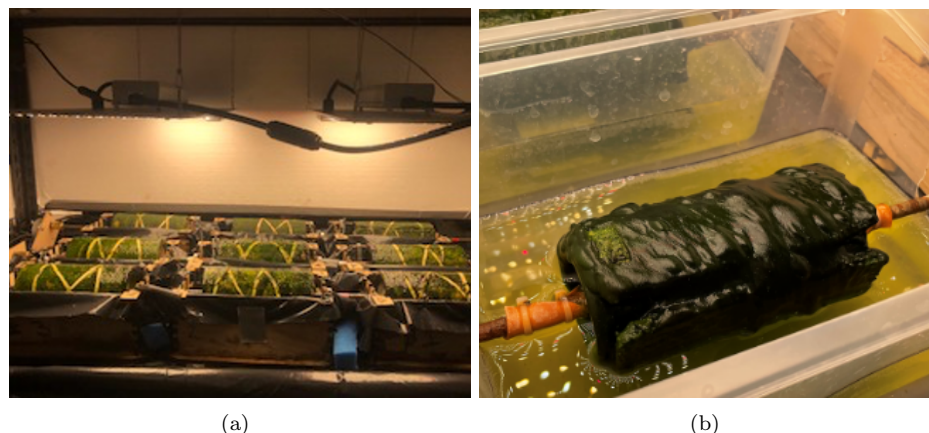


Figure 2.1: This figure provides an overview of the laboratory experiment setups for RABRs using 1 L of anaerobic digester effluent. Initially, the nine RABRs were constructed using wooden boxes lined with plastic with a photosynthetic photon flux density (PPFD) of $700\mu\text{mol}/(\text{m}^2\text{s})$, as illustrated in (a). Later on, the RABRs were transferred into plastic containers, as depicted in (b), with a higher PPFD of $1000\mu\text{mol}/(\text{m}^2\text{s})$.

Duty cycles (DCs) were selected as continuous rotation ($\text{DC} = 1$), 75% of time rotating and 25% no rotation ($\text{DC} = 0.75$), and 50% of time rotating and 50% no rotation ($\text{DC} = 0.5$). Triplicate RABRs were used to test each of the three DCs for the full duration of testing. The rotation rate was 6 RPM using a single-speed PolyVolt XMC-6035 motor. The temperature was maintained constant at $25^\circ\text{C} \pm 2^\circ\text{C}$. The RABRs were operated in batch mode, and algae biofilms were harvested every seven days when the media was replaced with new media. Anaerobic digester effluent served as the medium for algae cultivation. Hach Method #2606945 was used for ammonia analysis, and a Lachat QuikChem 8500 Series 2 instrument with method 10-115-01-3-A was used for total phosphorus analysis. The energy content of the algae biofilm was measured using bomb calorimetry.

Autotrophic Index. The Autotrophic Index (AI) is a measure that reveals the ratio of autotrophic and heterotrophic (microalgae) organisms within an algae biofilm community. It is calculated as the ratio of total dry biofilm biomass (heterotrophic + autotrophic) per unit biofilm area of a sample to the dry mass of chlorophyll a (autotrophic) extracted from the biomass per unit biofilm area [33], i.e.

$$\frac{\text{Total biomass including heterotrophs and autotrophs (kg/m}^2\text{)}}{\text{Mass of chlorophyll a (kg/m}^2\text{)}} = \text{AI}.$$

Thus, the autotrophic index values for a biofilm indicate whether or not the algae biofilm is autotrophic dominant. The AI value is unitless. AI values less than 200 typically indicate an

autotrophic-dominated biofilm, while higher values suggest increasing heterotrophic dominance. The procedure for the AI measurement [3] is provided in the supplementary materials.

Microalgae characterization. Microscopic characterization of biofilm microalgae was conducted to identify the types of microalgae present in the RABR biofilm visually. All microalgae were sourced from the Central Valley Wastewater Treatment Facility (CVWRF) trickling filters. Microalgae were observed using a compound light microscope to characterize the dominant types of microalgae present (green, cyanobacteria, diatoms) that remained consistent over time during the testing trials.

Measuring energy content of algae biofilm with bomb calorimetry. To determine the energy content of the algae biofilm, bomb calorimetry was utilized. It involves measuring the change in temperature for a 1 g dry mass sample of biofilm and the heat capacity for the calorimeter with the equation:

$$\Delta u = q := C\Delta T,$$

where C is the heat capacity with a unit $\text{kJ}/^\circ\text{C}$, ΔT is the temperature change with the unit $^\circ\text{C}$, and q is the heat released with a unit kJ/g which is equal to Δu , internal energy of the biofilm. The procedure of using the bomb calorimetry to measure the energy content [16] is provided in the supplementary materials.

Measuring biomass areal productivity. All the experimental data are collected from the experiment in Figure 2.1, except the biomass areal productivity. Because the biomass areal productivity, in particular the algae biofilm growth rate, shall be measured in a shorter time scale, we utilize another experiment, as shown in Figure 2.2, to estimate the areal productivity of algae biofilms on rotating algae biofilm reactors (RABRs). A growth platform of 0.7 m^2 of 4-ply cotton carpet with a plan view area of 2228cm^2 was placed on 4 RABRs and split into 32 sections. Three sections were sampled daily, with two sections sampled on day 11. The sections sampled were randomized to mitigate confounding factors. The RABRs were operated at a rotating velocity of 6 RPM with a photosynthetic photon flux density of approximately $600 \mu\text{mol}/(\text{m}^2\text{s})$. The temperature of the media was maintained at around $25^\circ\text{C} \pm 2^\circ\text{C}$. An anaerobic digester effluent was changed on day six of the experiment. Algae were sampled daily in appropriate sections and placed into labeled bags. Then, all algae were removed and dried on labeled aluminum pans in a 105°C oven. The weights were then measured, and the difference between the total weight and pan weight was recorded.

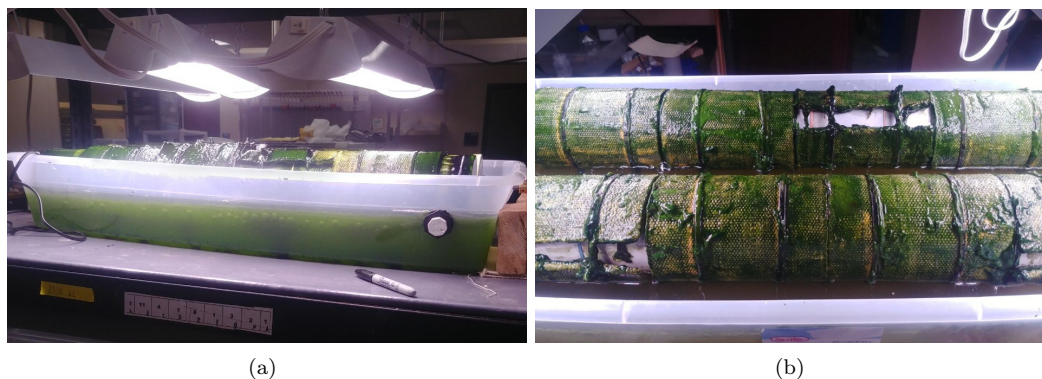


Figure 2.2: This figure shows a side view (a), and an aerial view (b) of some of the rotating algae biofilm reactors (RABRs) used to obtain empirical data on algae biomass growth. Four RABRs were placed within two 40L tanks containing anaerobic digester effluent. Three sections across RABRs were sampled daily over 11 days. A section was delineated by the black zip ties.

Energy efficiency. In industrial applications, areal productivity is the primary dependent variable of interest. However, it alone does not provide sufficient information for determining the design parameters of a RABR. Even though RABR is an energy-efficient system for cultivating microalgae to produce biomass for various applications, its energy cost shall not be ignored when compared with other bioreactors for biomass production. Mainly, the focus should not be solely on maximizing biomass production but rather on optimizing the biomass yield concerning the energy expenses associated with running a RABR. To address this, we introduce the energy efficiency metric Φ as $\Psi = \frac{Y}{P}$, where Y represents the RABR's yield and P denotes the power consumption of the RABR to achieve Y . The units for energy efficiency are $\text{kg}/(\text{m}^2\text{kW})$ and the derivations for total power are found in the supplementary materials section A.3. Negative values of energy efficiency will not be discussed in this paper and will be considered 0 for visualization and discussion purposes.

2.1.2 Mathematical model formulation

The experiments described above guide the development of this section's theoretical work. Our primary goal is to develop a predictive mathematical model that can be used to investigate the RABRs and provide theoretical insights on improving algae biomass areal productivity, nutrient uptake efficiency, and energy efficiency.

Photosynthetic mechanism. Given that light is the primary factor in algae biofilm areal productivity, we utilize the photosynthetic system [40] to model the algae biofilm photosynthetic process on the RABR. The photosynthetic process is assumed to have three physiological states, namely the reactive state in which the cell is ready to observe photons; the activated state, where the

cell processes solar energy into chemical energy; and the inhibited state in which the cell is dormant due to intense solar radiation, with volume fractions represented by A, B, and C, respectively. The inhibited state is assumed to recover to a reactive state once the light intensity is tolerable. On the RABR, the algae biofilm alternates between two distinct regimes, the water regime, and the air regime, as shown in Figure 2.3. During the photosynthetic process, the reactive state (A) is ready to absorb photons into the activated state (B). The activated state (B) is processing solar energy into chemical energy that will reproduce algae biofilms. Under intense solar radiation, the activated state (B) will transit into the inhibited state (C), a dormant status.

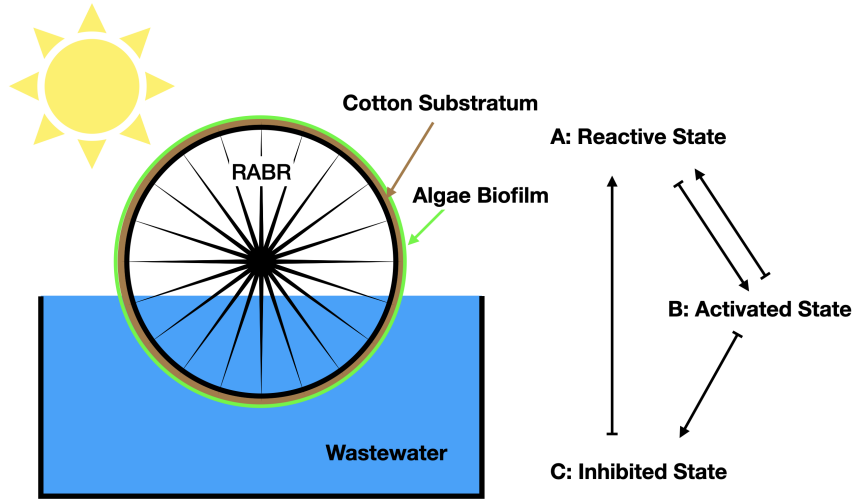


Figure 2.3: This figure depicts a schematic illustration of the rotating algal biofilm reactors (RABRs) and the photosynthetic system. The left panel shows a computational model proposed for RABRs, while the right panel illustrates the reactive kinetics taken from [40].

Through the mass action principle, the reactive kinetics for the three photosynthetic states, as summarized in Figure 2.3, are given as

$$\frac{dA}{dt} = -\sigma IA + \frac{B}{\tau} + k_r C, \quad (2.1a)$$

$$\frac{dB}{dt} = \sigma IA - \frac{B}{\tau} - k_d \sigma IB, \quad (2.1b)$$

$$\frac{dC}{dt} = -k_r C + k_d \sigma IB. \quad (2.1c)$$

In this context, k_r denotes the rate of repair, k_d represents the rate of damage, I is the light intensity, τ stands for the turnover time of the electron transport chain, and σ indicates the effective absorption cross-section per unit of photosynthetic units. Using the constraint $A + B + C = 1$, we can simplify

the reactive kinetics in (2.1) as

$$\begin{aligned}\frac{dB}{dt} &= \sigma I - \sigma I C - \left(\sigma I + k_d \sigma I + \frac{1}{\tau} \right) B, \\ \frac{dC}{dt} &= -k_r C + k_d \sigma I B.\end{aligned}\tag{2.2}$$

Biofilm thickness. Next, we consider the thickness of the biofilm and its effect on light attenuation. We will now assume that A , B , and C are functions of z and t where $z \in [0, h(t)]$ with $h(t) \geq 0$ the biofilm thickness. Denote the algae biomass concentration as $X(t)$ with units g/m^2 . We propose the algae growth rate to be determined by the following equation [4]

$$\frac{dX}{dt} = \left[\frac{1}{h} \int_0^h \mu(z, t) dz \right] X(t),\tag{2.3}$$

where $\mu(z, t)$ is the net growth rate, proposed as

$$\mu(z, t) = k \frac{B(z, t)}{\tau} - R(t),\tag{2.4}$$

based on the reactive kinetics in (2.1) with $R(t)$ the respiration rate and k a constant to scale the growth rate. We remark that k shall be determined with empirical studies of algae biofilm growth rates in laboratory settings. We assume $R(t) = R$ is a constant for simplicity.

Due to the thin nature of biofilm and to reduce the model complexity, we assume that the density of the algae biomass is uniform. This isotropic biofilm is assigned a density ρ , representing the algae biofilm's areal dry biomass density. Therefore, we can represent $X(t)$ as

$$X(t) = \rho h(t),\tag{2.5}$$

with $h(t)$ the height of the biofilm. Substituting (2.4) and (2.5) into (2.3), we obtain

$$\frac{dh(t)}{dt} = \int_0^h k \frac{B(z, t)}{\tau} dz - R h(t).\tag{2.6}$$

Light attenuation. With the introduction of biofilm thickness, we must now determine a relationship between light attenuation and the depth of the biofilm. Realistically, as one travels further within the biofilm, the available light for each photosystem of the cell will decrease. One of the most widely used equations to model this relationship, and the choice for our model, is Beer Lambert's law [4]. Let $\hat{I}(t)$ be the surface light intensity at time t and let b be a constant representing

the light attenuation factor. Then, the available light at time t and depth z is represented as

$$I(z, t) = \hat{I}(t)e^{-b(h-z)}, \quad z \in [0, h]. \quad (2.7)$$

As the RABR rotates, a proportion of the surface will be exposed to the sunlight, while the rest will be immersed underwater. Then, we introduce the variables L to be the circumference of the RABR and l_* the exposed length. We denote the peripheral velocity of the RABR as v and the period of the RABR as T . Then the peripheral velocity v , length L , and period T have the relation: $T = \frac{L}{v}$. Then the actual light intensity can be modeled by a square wave defined as

$$\hat{I}(t) = \hat{I}_0(t)\Gamma(t), \quad \Gamma(t) = H\left(\text{mod}(t, T) - \frac{l_*}{L}\right), \quad (2.8)$$

with $\hat{I}_0(t)$ the maximum light intensity and H is the Heaviside step function.

Nutrient uptake. The algae biofilm shall be regularly exposed to adequate nutrients to accumulate biomass, which is then absorbed through nutrient mass transport. Let us denote $E(z, t)$ as the nutrient concentration in the biofilm with depth z at time t with $0 \leq z \leq h$. To simplify the model, we assume that the nutrient concentration $E(z, t)$ is homogeneous at different depths of the algae biofilm, i.e., E is only a function of time. When the algae biofilm is within the water, nutrients are replenished. When the algae biofilm is in the air, the nutrient is consumed. Therefore, we propose the governing equation for the nutrient on the RABR as

$$\frac{dE(t)}{dt} = -\gamma_{a1}\Gamma(t)\frac{E(t)}{K_a + E(t)}\frac{1}{h}\int_0^h B(z, t)dz - \gamma_{a2}(1 - \Gamma(t))(E(t) - E_T(t)), \quad (2.9)$$

where $E_T(t)$ is the nutrient concentration in the water at time t , and γ_{a1}, γ_{a2} control the nutrient uptake and intake rates, and K_a is the half-saturation constant.

When the nutrient in the wastewater is abundant, we can assume $E_T(t)$ as a constant. When the nutrient in the wastewater becomes a limiting factor, the dynamics for $E_T(t)$ shall be considered. Next, let us consider the finite nature of the nutrients available to the RABR. When the RABR is within the water, nutrients are taken from the water into the algae biofilm. The uptake rate is a function of both the current mass of algae biofilm present and the proportion of algae biofilm converting itself into algae biomass in the B state, i.e. activated state.

Therefore, we propose the governing equation for E_T as

$$\frac{dE_T(t)}{dt} = \gamma_T \frac{Sh}{V} (1 - \Gamma(t)) (E(t) - E_T(t)), \quad (2.10)$$

where V is the volume of the waste water container, Sh represents the total volume of biomass on the RABR, and γ_T is the effective nutrient consumption rate for the system.

Water evaporation. When the RABR rotates slowly or when the RABR is idle during the duty cycle, part of the algae biofilm is exposed to the air for a prolonged period of time. In such situations, the effect of water evaporation on algae biofilm growth and mortality shall be taken into account.

We introduce $W(t)$ as the water saturation percentage. In the water, $W(t) = 1$, and outside of the water, $W(t)$ is a monotone decreasing function of time. The governing equation for algae biofilm growth would be updated as

$$\frac{dh(t)}{dt} = \int_0^{h(t)} k \frac{B(z, t)}{\tau} \frac{E(t)}{K_a + E(t)} \frac{\frac{3}{2}W(t)}{K_W + W(t)} dz - \left(R + R_W \frac{K_W}{W(t) + K_W} \right) h(t), \quad (2.11)$$

where K_W is the critical water stress threshold for algae biofilm growth. The term $\frac{W(t)}{K_W + W(t)}$ represents the water stress on algal biofilm growth, $\frac{K_W}{W(t) + K_W}$ represents the water stress on algal biofilm death, and R_W is the extra death rate. The governing equation for $W(t)$ is proposed as follows

$$\frac{dW(t)}{dt} = -\gamma_{w1}\Gamma(t) \frac{W(t)}{K_W + W(t)} - \gamma_{w2} \left(1 - \Gamma(t) \right) \left(W(t) - 1 \right), \quad (2.12)$$

where γ_{w1} is the water evaporation rate and γ_{w2} is the absorption rate from the wastewater.

2.2 Results

The flexibility of the laboratory setups allows us to design specific experiments to investigate algae biomass areal productivity and nutrient uptake rates, which are then used to refine the mathematical models for predicting theoretical results. In this section, we summarize our experimental and theoretical findings, with a focus on key parameters of interest, such as biomass areal productivity and nutrient uptake efficiency.

Autotrophic Index. Results of AI testing over a two-week experiment shown in Figure 2.1 are summarized in Table 2.1 and indicate that autotrophs (microalgae) dominated the biofilm compared with heterotrophs (bacteria) present in the biofilm.

Table 2.1: Autotrophic Index values for biofilm samples in different duty cycles.

Days of Testing	Duty Cycle = 0.50	Duty Cycle = 0.75	Duty Cycle = 1.00
Initial	33 ± 1.08	40 ± 1.18	25 ± 0.23
7	29 ± 0.63	35 ± 1.57	20 ± 0.43
14	20 ± 0.49	26 ± 0.69	16 ± 0.23

Microalgae characterization. Microscopic characterization of the predominant microalgae that were present in the biofilms is shown in Table 2.2. There were no qualitative differences among the individual replicate RABRs.

Table 2.2: Microscopic characterization of algae biofilm. This table summaries the identified algae and Cyanobacteria.

Appearance	Name
Single	Chlorella
Single	Chlorococcum
Filamentous	Ulthorix
Filamentous	Lyngbya
Filamentous	Odogonium
Diatom	Gomphonema

Energy content of algae biofilm. Table 2.3 presents the results of the bomb calorimetry analysis conducted to determine the energy content of the algae biofilm.

Table 2.3: Areal energy content of biofilm microalgae (kJ/m^2)

Duty Cycle = 0.50	Duty Cycle = 0.75	Duty Cycle = 1.00
250	305	360

Biomass areal productivity. The areal productivity was calculated for each sample by dividing the dried algae biomass by the elapsed time and plan view area in the experiment shown in Figure 2.2. The collected data is summarized in Figure 2.4. We find that the growth rate $k = 5 \times 10^{-5}$ is a reasonable choice by fitting the model with the experimental data. As shown in Figure 2.4, the model prediction agrees well with the experimental data.

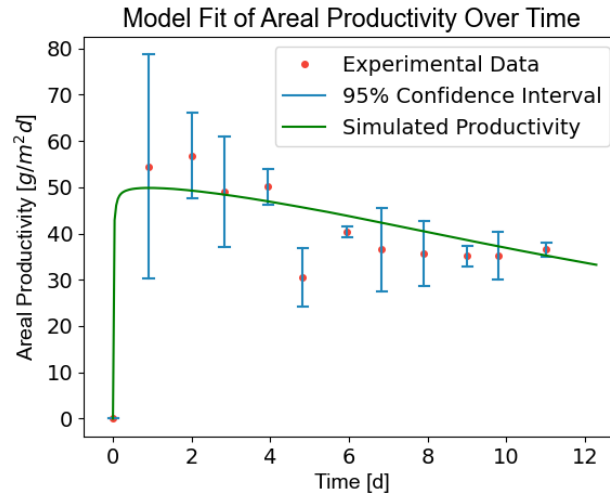


Figure 2.4: This figure shows the areal productivity of the four rotating algae biofilm reactors (RABRs) over an 11-day experiment, measured in units of $\text{g}/(\text{m}^2\text{d})$. The experiment involved a change in anaerobic digester effluent on day 6. The confidence intervals (95%) were constructed using the triplicate measurements obtained on each day. A parameter study on the growth rate k indicated that $k = 5 \times 10^{-5}$.

Nutrient uptake. After 30 days to attain steady state operation, approximately 25 days were selected to measure the effluent of the nine RABRs. The influent and effluent samples were measured for ammonia levels during the experiment, as shown in Figure 2.5. Each effluent sample was measured in triplicates and then averaged.

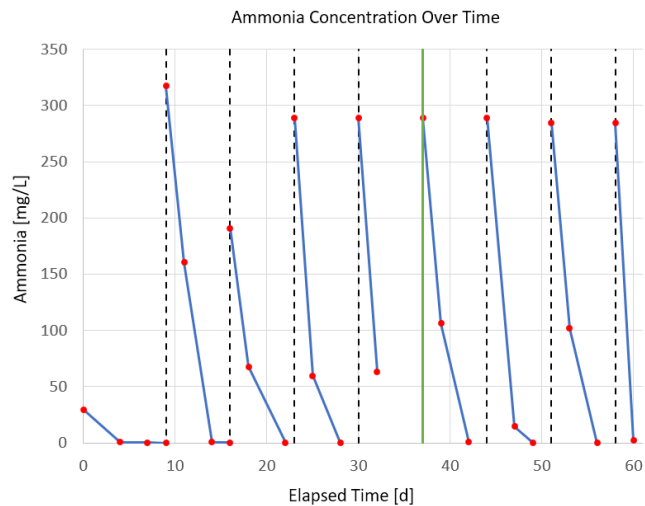


Figure 2.5: A timeline of the ammonia effluent levels throughout the experiment. Black dotted lines correspond to a replacement of anaerobic digester effluent, and the red line corresponds to the parameter change of $700 \mu\text{mol}/(\text{m}^2\text{s})$ to $1000 \mu\text{mol}/(\text{m}^2\text{s})$.

The ammonia samples were grouped by their sampling time relative to the most recent re-

placement of influent to condense and synthesize the data. Additionally, previous testing in our lab demonstrated that factor levels of the duty cycle had no obvious correlation with the dependent variables studied. We grouped all factor levels of the duty cycle for our nutrient data. Let Day 0 represent the day on which anaerobic digester effluent is replaced for each RABR. Day N is the Nth day after the most recent influent replacement in which the effluent was measured. Additionally, data was initially split into two parts, as this corresponded to an adjustment of 700 to 1000 $\mu\text{mol}/(\text{m}^2\text{s})$ for incident light. The visualization of the regrouped data is shown in Figure A.2. Since there is no significant difference in the trends of nutrient depletion for 700 and 1000 $\mu\text{mol}/(\text{m}^2\text{s})$, we combine all the ammonia data by taking the average of the ammonia concentration on the Nth day for all light regimes. Similar to ammonia, the phosphorus data values were grouped by their relative sampling time from the most recent influent replacement while ignoring factor levels of PPF and duty cycle. The data are presented in Figure A.2.

For $E_0 = 283.1\text{mg/L}$ (ammonia) to reach less than 1mg/L (the value for the half-saturation constant of ammonia) in 8 hours, we select γ_{a1} to be $1470\text{mg}/(\text{Ld})$ for ammonia. For $E_0 = 14.1\text{mg/L}$ (phosphorus) to approach below 0.04mg/L (the value for the half-saturation constant of phosphorus) in 8 hours with our conditions, we select γ_{a1} to be $73\text{mg}/(\text{Ld})$. Figure 2.6 shows that the model prediction agrees well with the experimental data.

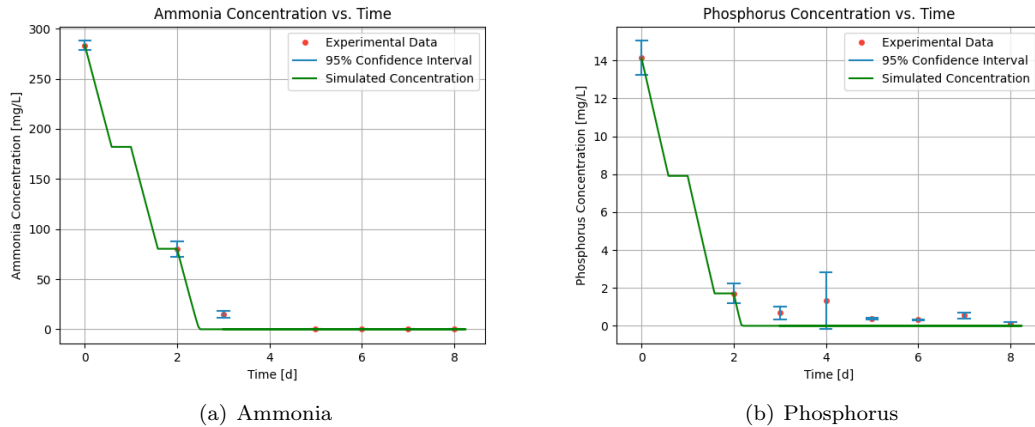


Figure 2.6: This figure shows the total nutrient depletion over time for ammonia (a) and phosphorus (b). Parameter fittings for the total nutrient depletion rate γ_T indicates that $\gamma_T = 8.47 \times 10^9 \text{d}^{-1}$ for ammonia, and $\gamma_T = 1.764 \times 10^{10} \text{d}^{-1}$ for phosphorus.

Although both ammonia and phosphorus are present in the algae biofilm on the RABR, it is phosphorus that limits the growth of algae. While the nitrogen-to-phosphorus molar ratio for algae is 16:1, the ratio in the anaerobic digester effluent is 22:1, indicating an excess of nitrogen relative

to phosphorus. Therefore, in the subsequent sections of this paper, we focus on phosphorus as the limiting nutrient and use nutrient parameters specific to phosphorus in our simulation results.

Numerical studies of the operation parameters and nature conditions. Eight hundred sixty-one simulations were conducted as a parameter study for peripheral velocity and PPF to investigate their effects on the RABR's function. The parameters used to produce these figures are taken from the parameter tables in the supplemental materials. First, the algae biofilm thickness on the RABR over time is summarized in Figure 2.7. The supplemental materials in Figure A.7 summarize a different visualization using contour plots.

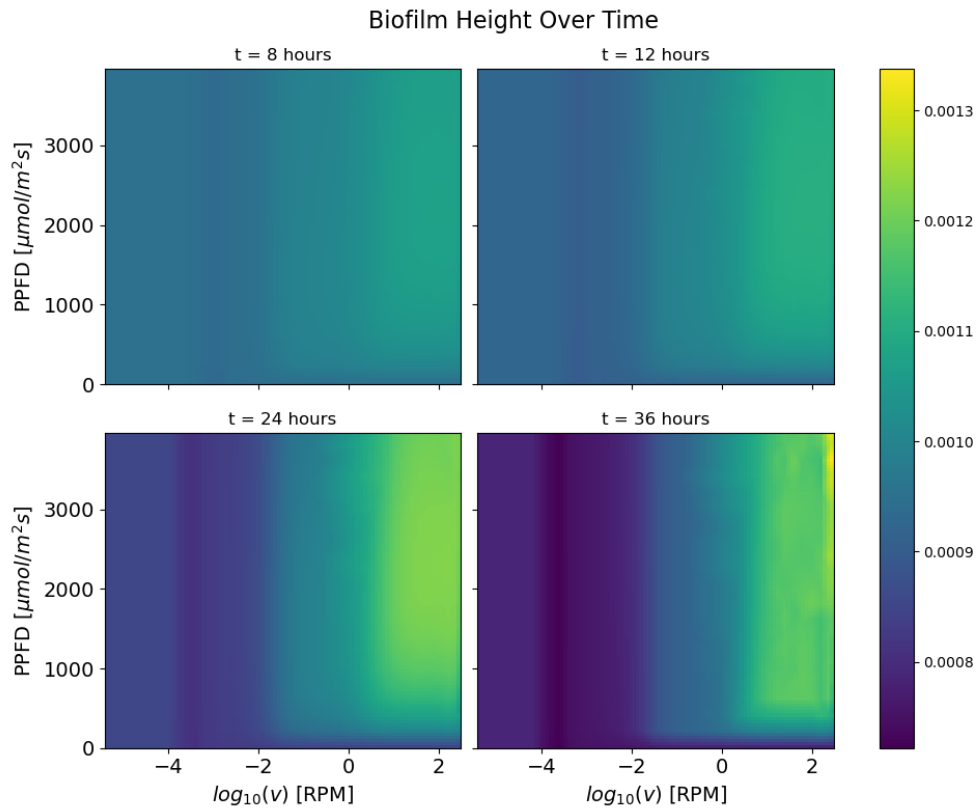


Figure 2.7: This figure displays the growth of algae biofilm over time under varying peripheral velocity (RPM) and photosynthetic photon flux density (PPFD) conditions. The algae biofilm heights over time at $t = 12, 23, 36,$ and 48 hours are shown.

The algae biofilm areal productivity of the RABRs is recorded through the eight hundred sixty-one simulations as well. Areal productivity is calculated as the change of yield in equation (2.5) over the elapsed time in the simulation. The results are summarized in Figure 2.8. A different visualization using contour plots can be found in the supplemental materials in Figure A.8.

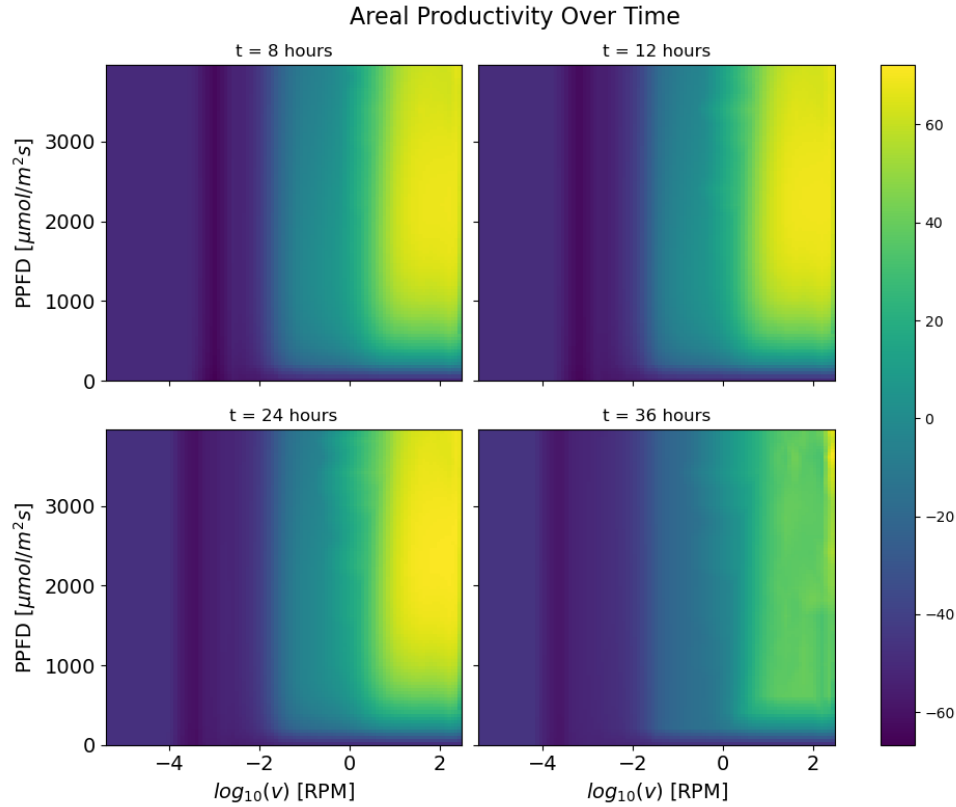


Figure 2.8: This figure presents snapshots of algae biofilm areal productivity at 12-hour intervals over time. It shows the effects of varying peripheral velocity (RPM) and photosynthetic photon flux density (PPFD) on algae biofilm areal productivity through a parameter study.

Along with biomass areal productivity, nutrient uptake efficiency from the wastewater is another crucial factor in the RABR design and operation. We simulate the nutrient uptake under various peripheral velocities and PPF conditions in the same setting. The results are summarized in Figure 2.9. The supplemental materials in Figure A.9 summarize a different visualization using contour plots.

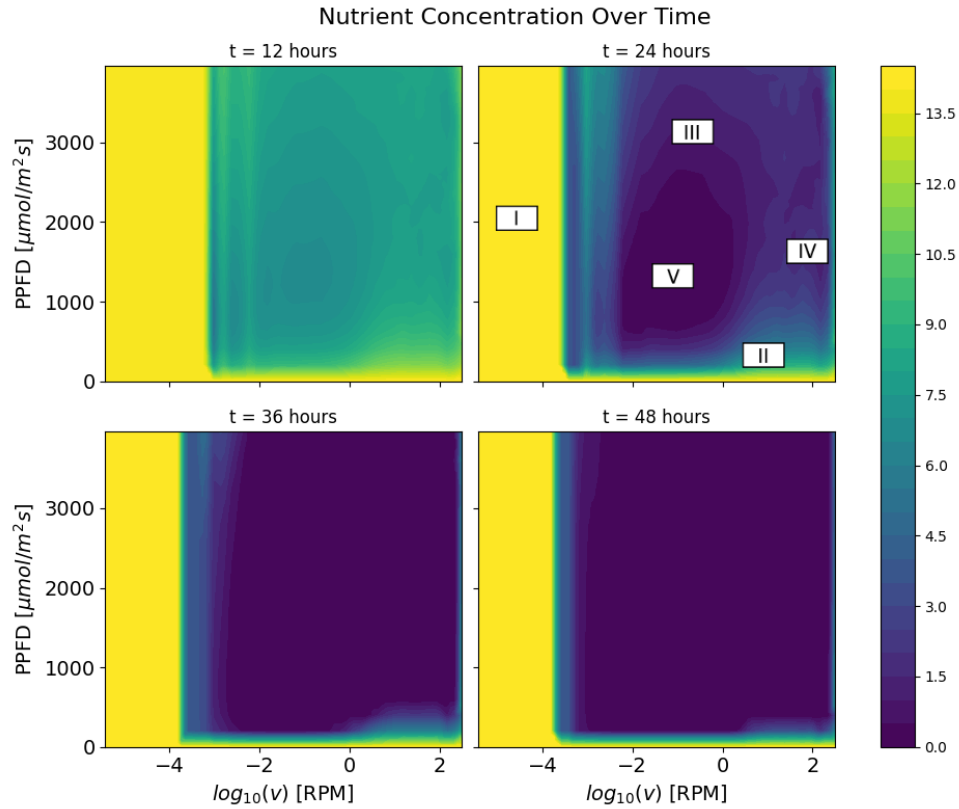


Figure 2.9: This figure illustrates the changes in nutrient concentration over time under different peripheral velocities (RPM) and photosynthetic photon flux density (PPFD) conditions, as determined by a parameter study.

Next, we conduct several numerical investigations on energy efficiency. Our goal is to identify the effect of duty cycle and peripheral velocity on energy efficiency, thus identifying the optimal operating parameters to maximize energy efficiency. Another parameter study of eight hundred sixty-one simulations determining the energy efficiency under different light intensities with 700, 1000, 2000, and 3000 PPFD are summarized in Figure 2.10.

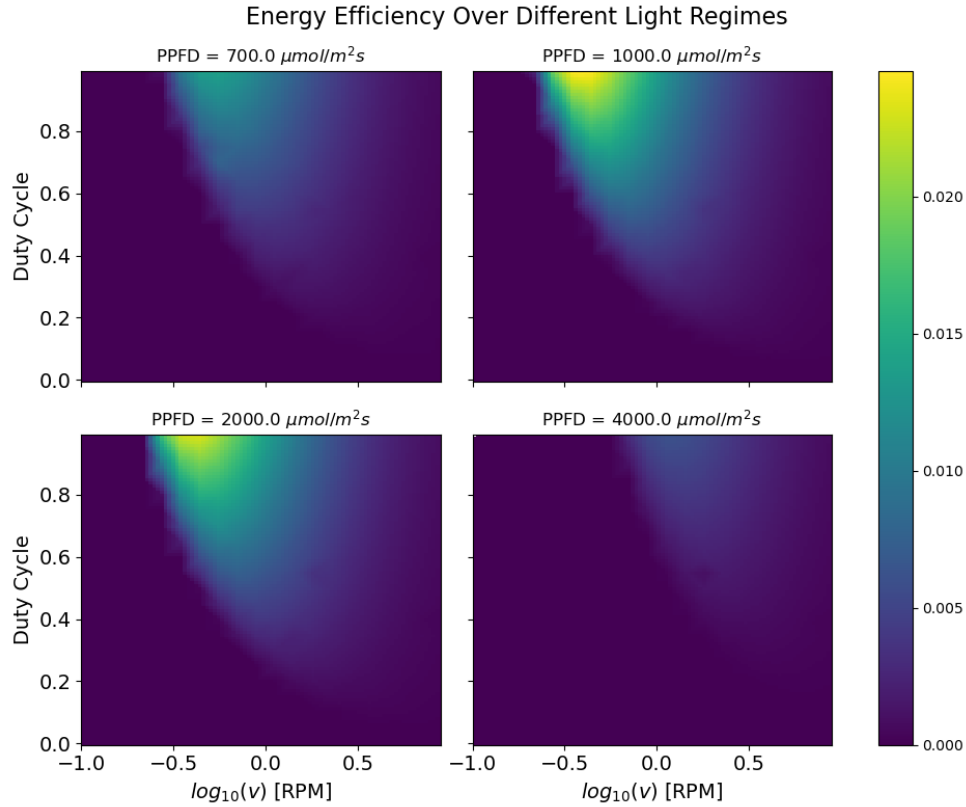


Figure 2.10: This figure shows the energy efficiency plotted against duty cycle and velocity, with a duty cycle period of 60 seconds, utilizing parameters provided in the tables.

To better visualize the results above, we conduct another eight hundred sixty-one simulations and plot several cross-section views for the energy efficiency under various light intensities as shown in Figure 2.11. Specifically, we fixed the duty cycle as 0.2 and 0.8, then we investigate the energy efficiency under various peripheral velocities, and then we fixed the peripheral velocity to values of $-0.5\log_{10}$ and $0.5\log_{10}$ RPM, to investigate the energy efficiency under various duty cycles.

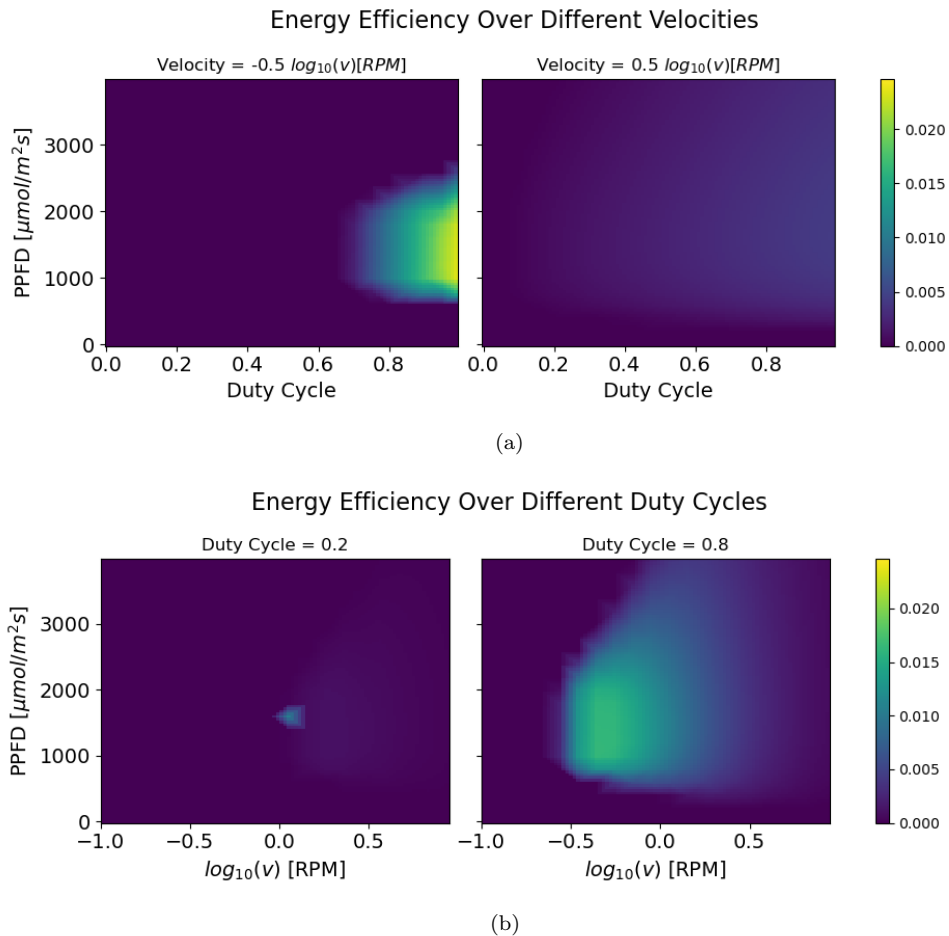


Figure 2.11: This figure shows the energy efficiency at various operational settings. Here we fixed duty cycle period as 60 seconds and use the same parameters provided in the tables.

Additionally, one notices that the duty cycle alone can't uniquely determine the operational settings. An extra freedom is the duty cycle period, i.e. the period for each cycle. Hence, we further conduct a numerical study for the energy efficiency under different duty cycle periods in a total of eight hundred sixty-one simulations. The numerical results are summarized in Figure 2.12.

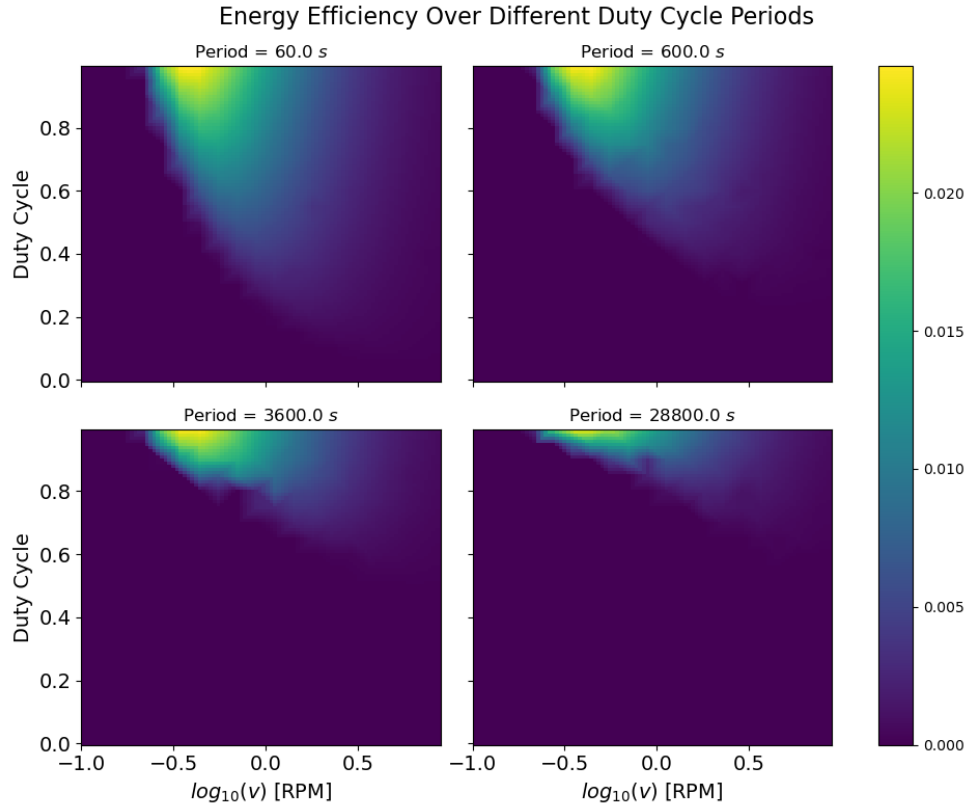


Figure 2.12: This figure shows the energy efficiency under various duty cycle periods. All the parameters are the same as in the previous study except for the duty cycle period.

2.3 Discussion

RABRs present a promising technology for sustainable algae-based production systems, with potential applications in biofuel production, wastewater treatment, and aquaculture. In addition to their applications, RABRs also present several challenges and limitations. One challenge is optimizing the system's design and operation for maximum areal productivity and nutrient uptake while minimizing energy consumption and environmental impact. To address this question, we have developed a unified experimental and theoretical approach by designing lab-based experimental setups accompanied by computational mathematical models.

The laboratory experiment shown in Figure 2.1 enabled us to measure the energy content of the algae biofilm and the nutrient consumption rate of the RABR under various operational and environmental conditions. The results presented in Table 2.3 demonstrate that the energy content of the biofilm increases with duty cycle value, likely due to higher areal productivity with longer exposure times to light energy.

Meanwhile, it is worth pointing out that the rapid decrease of concentrations shown in Figure 2.6 for both ammonia and phosphorus is due to nutrient uptake from the algae biofilm. In addition, for pH values greater than 9.3, such as the environment of the RABR, ammonia can volatilize and be removed from the anaerobic digester effluent in the RABR [14]. For phosphorus, removal in the water phase can occur in the form of struvite precipitation in basic environments.

Our numerical study shows that one must carefully select an optimal value for PPFD to maximize algae-based biomass over time. For instance, at $t = 36$ hours in Figure 2.7, one can see several regions with weak, medium, and strong light intensities. Figure 2.8 also indicates an optimal PPFD value for areal productivity and reflects three light regimes as well. In particular, with the lack of incident light, the algae biofilm growth is limited. With the incident light strong, the peripheral velocity plays a crucial role, as illustrated in Figure A.3. The algae biofilm has little time to be overexposed and is always near a recovery time in the water with a fast velocity. These findings indicate that maximal areal productivity depends both on light intensity and RABR peripheral velocity. They also indicate that a velocity of around 10 rotations per minute would lead to relatively good areal productivity.

Meanwhile, we observe a positive correlation between peripheral velocity and algae biomass growth and areal productivity. When velocity is slower than one rotation every 90 minutes, the effect of water evaporation will limit or completely stop biofilm growth, as the algae biomass will be dry and run out of present water and nutrients. On the other hand, a faster velocity will correspond with an increase in algae biomass regardless of the light regime. The reason for this strong correlation lies within the activated state (B state) values of the algae biofilm. Recall that one of the main factors determining algae biofilm growth rate is the average value of the activated state (B state) within the algae biofilm. To justify this hypothesis further, we present the proportion of algae within the activated state (B state) for two choices of RABR velocity in Figure A.3. We observe that the average activated state values among the biofilm are recorded for a "slow" velocity of 0.0375 RPM and a "fast" velocity of 375 RPM. When the RABR biofilm is within the media, the algae has no access to sunlight, so the activated state present converts to the reactive state (A state). However, when spinning quickly, the biofilm within the activated state has little time to convert to the reactive state by the time the RABR biofilm is again exposed to the incident light in the air regime, causing the proportion of algae in the activated state to stay relatively high. This effect is more or less pronounced depending on how fast or slow the RABR rotates.

Our results indicate that maximal areal productivity depends on light intensity and RABR peripheral velocity. Interestingly, we observe that nutrient uptake as a function of peripheral velocity

and PPFD differs greatly from the areal productivity results. Figure 2.9 shows five regions of interest to consider. The first two areas to examine are those with little to no nutrient uptake occurs. This happens in both regions I and II in Figure 2.9. For velocities slower than one rotation every 90 minutes (region I), mechanics such as water evaporation and mass transport will limit algae biofilm growth. When the RABR spins too slowly, evaporation inhibits growth, and/or the algae biofilm runs out of nutrients and starves. The other area with little to no nutrient uptake occurs when PPFD is near $0 \mu\text{mol}/(\text{m}^2\text{s})$, labeled as region II. With no incident light, algae biofilm growth does not occur. For both areas in which the velocity of incident light is too little, as algae biofilm growth is limited or stopped, the rate of nutrient uptake in (2.10) becomes 0 as the biofilm height approaches zero. Region III is the area where velocity is greater than one rotation every 90 minutes and light intensity is greater than $2500 \mu\text{mol}/(\text{m}^2\text{s})$. Within this region, algae biofilm growth is present but limited by photoinhibition. Due to this reduced potential of algae biomass, the nutrient uptake is present but not optimal. The next region consideration is where areal productivity/algae biomass growth is optimized, denoted as region IV. As discussed earlier in Figures 2.7 and 2.8, this region is where incident light is between 1000 and $2000 \mu\text{mol}/(\text{m}^2\text{s})$ and velocity is greater than 10 rotations per minute. This region has better nutrient uptake than the previously discussed regions, as the algae biomass is greatest within this region.

The final and most interesting region to consider is region V where PPFD is in an optimal range, but velocity is slower and approximately one rotation every 90 minutes. By comparing the results in Figure 2.8 and 2.9, our results indicate that the region of optimal nutrient uptake does not correspond with optimal algae biofilm growth. An additional consideration of an optimal velocity must be accounted for in determining optimal nutrient uptake. Further, for any light regime, the optimal nutrient uptake does not lie where velocity is maximized.

The driving mechanism for slower velocities corresponding to faster nutrient uptake is the term $(E - E_T)$ found in (2.10). When the RABR spins slowly, there is a lot more time for mass transport and digestion of the nutrient to occur within the algae biofilm, so when reintroduced into the media, the difference in nutrient concentrations between the algae biofilm and media is large. Compared to a faster velocity, this large discrepancy then drives a relatively quicker nutrient depletion within the media. With our assumptions of first-order kinematics, this discrepancy widens much quicker than a faster velocity can compensate. For illustration purposes, Figure A.4 demonstrates this difference between two simulations: 375 RPM and 0.0375 RPM.

Next, we discuss our findings regarding energy efficiency. As illustrated in Figure 2.10, the optimal energy efficiency significantly deviates from the optimal operational factors for areal produc-

tivity. We observe a distinct nonlinear crescent shape representing optimal efficiency, which shifts and compresses under different light conditions. We posit the general shape is that of a crescent as we assume linear increases in velocity and duty cycle correspond to quadratic and linear increases in energy costs, as demonstrated in equation (A.4). For higher velocities, a lower duty cycle is optimal for energy efficiency as the increased rotational velocity compensates for the periods of inactivity of the RABR and allows the algae to survive. Conversely, as velocity decreases, a higher duty cycle is required for optimal efficiency, as slower speeds demand higher duty cycles to prevent the algae biofilm from dying. At $-0.5 \log_{10}$ RPM (approximately one rotation every three minutes), a duty cycle of 1 is necessary since anything less becomes lethal to the algae biofilm, and the reduced energy costs would not compensate for the reduced algae biofilm yield. Beyond a certain point, if the peripheral velocity is too slow, no duty cycle can keep the algae biofilm alive. As velocity increases, energy efficiency decreases. The algae biomass yield gains from faster velocities do not increase as rapidly as the associated energy costs. For any given velocity, an optimal duty cycle exists, and for any duty cycle, an optimal velocity exists. The discrepancies in the magnitude of efficiency across the four subfigures in 2.10 primarily stem from varying algae biofilm yields. Among them, a light intensity of 1000 and 2000 PPFd produce the best algae biofilm yield, as 700 PPFd limits photosynthesis and 4000 PPFd accelerates photoinhibition within the algae biofilm.

The results presented in Figure 2.11 allow us to examine the differences in energy efficiency across various light regimes. First, let us fix velocity at a relatively slow velocity at $-0.5 \log_{10}$ RPM, or approximately one rotation every 3 minutes. As shown in the left figure in subfigure (a), for all studied light regimes, the optimal duty cycle is 1. For light regimes suboptimal to biofilm growth (PPFd less than 1000 or greater than 2000), duty cycle becomes more sensitive to determining the optimal energy efficiency. In contrast to these findings, when fixing peripheral velocity to a relatively fast velocity at $0.5 \log_{10}$ RPM, or approximately 3 RPM, the parameters of duty cycle and PPFd matter little to optimizing energy efficiency. At these speeds, any tuning of duty cycle and PPFd will not compensate for the high energy costs of rotating the RABR.

Next, observe subfigure (b) of Figure 2.11 in which duty cycle is fixed and velocity and PPFd are varied. Similar to when fixing peripheral velocity at $0.5 \log_{10}$ RPM, fixing duty cycle at 0.2 lends to peripheral velocity and PPFd having little effect on energy efficiency. With the exception of needing to keep velocity faster than 1 RPM, the energy efficiency is relatively constant among the observed variables as at such a low duty cycle, biomass growth is stagnated. A much more interesting relationship between peripheral velocity and PPFd occurs when one fixes duty cycle to be 0.8. At a higher duty cycle, optimal energy efficiency occurs at a velocity of $-0.5 \log_{10}$ RPM.

Anything slower will be lethal to the biofilm and energy efficiency is 0. For PPFD values below 1000, not enough light is present in the system, and biomass growth is limited or nonexistent, leading to 0 energy efficiency. As PPFD increases, the corresponding peripheral velocity that optimizes energy efficiency increases.

Observed from Figure 2.12, when the duty cycle period increases, the energy efficiency becomes more sensitive to duty cycle. As the duty cycle period increases, the time in which the RABR is not spinning when turned off by the duty cycle increases, making such occurrences more punishing for algal growth. Therefore, for high duty cycle periods, one must keep duty cycle close to 1. To have more flexibility on duty cycle, the duty cycle period must be small.

We point out that there are several limitations to our model. We don't consider inertia and related algae biofilm sloughing in our current model, which will rule out selections of unreasonably fast velocities. Furthermore, cell death due to environmental constraints such as strong heat and its effects on mass transport is not considered in this current model. These issues will be further addressed in our later research projects.

Another limitation of our model is the methods by which we calculate energy costs for the RABR. Our energy calculations are based on the moment of inertia of a hollow cylinder and a constant overhead energy cost independent of the duty cycle or peripheral velocity. Within our calculation, mass is assumed to be constant, and friction between the anaerobic digester effluent and substratum is assumed to be 0. Additionally, we do not consider the energy costs to toggle the power of the RABR, leading to identical energy costs for all choices of the duty cycle period. For future implementations of our model, we recommend developing one's own function for energy costs that are tailored to the specific design at hand. We argue that one will find similar trends when optimizing energy efficiency along the variables of peripheral velocity, PPFD, duty cycle, and duty cycle period.

CHAPTER 3
EXPLORING MICROALGAE GROWTH IN HETEROGENEOUS ROTATING ALGAL
BIOFILM REACTORS (RABR) THROUGH COMPUTATIONAL MODELING

Despite the significance of spatial heterogeneity in RABR systems, there is limited research exploring its impact on biomass productivity, which serves as the motivation for this study. Specifically, our objectives include advancing the theoretical capabilities of the photosystem model from our previous work, integrating a spatial component into biofilm modeling to highlight the algae variability across the growth substratum surface, simulating non-uniform environments and stimuli affecting the biofilm, and contrasting the effects of natural sunlight and laboratory LED photosynthetic photon flux density (PPFD) on biofilm cultivation.

3.1 Mathematical Model Formulation

In this section, we provide a detailed derivation for the mathematical model following the inclusion of spatial heterogeneity. Since light is the primary factor in algae biofilm productivity, we utilize the photosynthetic system introduced in [40]. The algae biofilm alternates between two distinct regimes (Figure 3.1). The first regime is the water regime, where we assume that algae biomass will be converted to the open (A) state. The second regime is the air regime in which biomass will generally be converted either to the closed (B) state or inhibited (C) state.

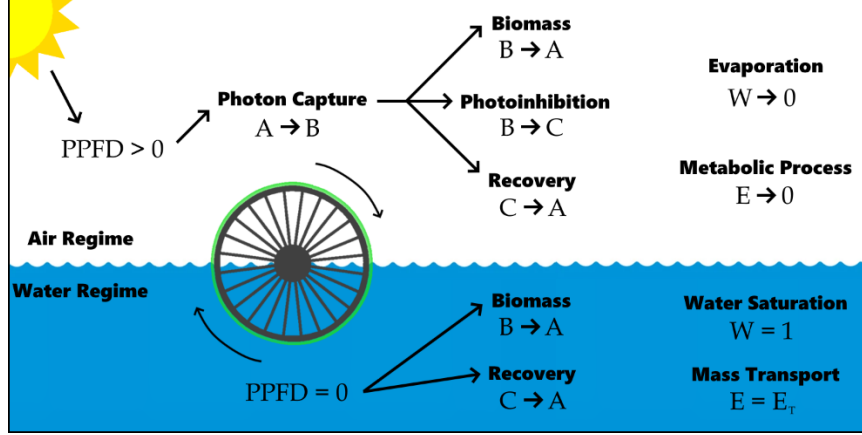


Figure 3.1: A schematic illustration of the rotating algal biofilm reactors (RABR) and the photosynthetic system. This figure illustrates the proposed computational model for the rotating algal biofilm reactor (RABR) on the left.

3.1.1 Photosynthetic kinetics with spatial heterogeneity

Consider a substratum with length L . We introduce the spatial variable x , $0 \leq x \leq L$ to represent the spatial location of the substratum. We introduce the notations $A(x, z, t)$, $B(x, z, t)$ and $C(x, z, t)$ to represent the volume fractions of A, B, C states at location x and height z , where $z \in [0, h(x, t)]$ with $h(x, t)$ the thickness of biomass at location x and time t .

The original RABR model [4, 40] can be extended as

$$\partial_t A(x, z, t) = D_a A_{xx} - \sigma I(x, z, t) A(x, z, t) + \frac{B(x, z, t)}{\tau} + k_r C(x, z, t), \quad (3.1a)$$

$$\partial_t B(x, z, t) = D_b B_{xx} + \sigma I(x, z, t) A(x, z, t) - \frac{B}{\tau} - k_d \sigma I(x, z, t) B(x, z, t), \quad (3.1b)$$

$$\partial_t C(x, z, t) = D_c C_{xx} - k_r C(x, z, t) + k_d \sigma I(x, z, t) B(x, z, t), \quad (3.1c)$$

where $x \in [0, L]$, $z \in [0, h]$, and D_a, D_b , and D_c represent the passive diffusion between the A, B, and C states. Here $I(x, z, t)$ represents the light intensity that will be elaborated on later. The parameters σ, k_r, k_d controls the rates between the three states [40, 4].

Due to the incompressibility, we have the constraint

$$A(x, z, t) + B(x, z, t) + C(x, z, t) = 1, \quad \forall (x, z, t) \in [0, L] \times [0, h(x, t)] \times [0, T],$$

which leads to

$$\partial_t [A(x, z, t) + B(x, z, t) + C(x, z, t)] = 0.$$

Adding the equations in (3.1), it leads to $D_a A_{xx} + D_b B_{xx} + D_c C_{xx} = 0$. For simplicity, we assume that $D_a = D_b = D_c$ in this paper.

3.1.2 Light mechanism

As the RABR rotates, a proportion of the surface will be exposed to the sunlight, while the rest will be immersed underwater. Recall L represents the circumference of the RABR (the length of the substratum). We denote l_* the exposed length. We denote the peripheral velocity of the RABR as v and the period of the RABR as T . Then the peripheral velocity v , length L , and period T have the relation:

$$T = \frac{L}{v}. \quad (3.2)$$

Since the substratum is a closed loop, ideally, the spatial variable could be defined in real space with a period of L . Define the flag function

$$\Gamma(x, t) = f(\text{mod}(x + vt, L)), \quad f(x) = \frac{1}{1 + e^{-\frac{x - r_0 L}{\epsilon}}}. \quad (3.3)$$

Here $f(x)$ is the logistic function, ϵ controls the transition thickness of the S curve, and r_0 is the ratio of substratum exposure to the air. Γ function is the flag to mark whether the location x at time t is exposed to the air when $\Gamma(x, t) = 1$, or not when $\Gamma(x, t) = 0$.

Then, we model the surface light intensity. The actual light intensity can be modeled by a square wave defined as

$$\hat{I}(x, t) = \hat{I}_0(t)\Gamma(x, t), \quad (3.4)$$

with $\hat{I}_0(t)$ the maximum light intensity. There are several approaches to approximate $\hat{I}_0(t)$. For our model, we utilized existing light intensity data on April 25th, 2018, collected from the Sustainable Waste-to-Bioproducts Engineering Center (SWBEC). The light intensity is measured as photosynthetically active radiation (PAR) every 15 minutes for 24 hours. We then fit the PAR data with a smooth function $\hat{I}_0(t)$ as shown in Figure 3.2 for a range of one day. Moreover, we let $t = 0$ within our simulations correspond to 8:00 AM with the function, and we assume each day has the same light pattern when simulating for a more extended period.

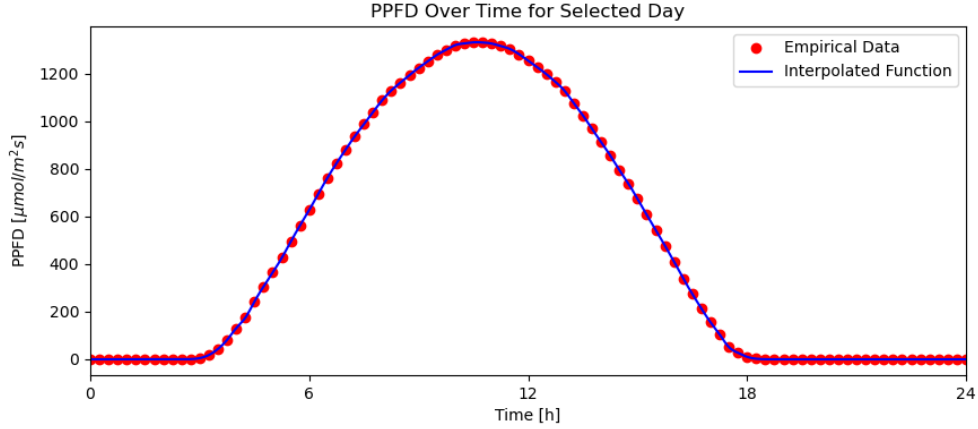


Figure 3.2: Light intensity over time. The figure illustrates 24-hour PAR data as red points, with a fitted continuous function represented by a blue curve. This continuous function will be employed for subsequent simulations, starting at $t = 8$ hours for the interpolated function within the model for simulations.

Incorporating biofilm thickness necessitates establishing a connection between light attenuation and biofilm depth. Intuitively, as one delves deeper into the biofilm, the accessible light for each cell's photosystem diminishes. A widely adopted equation to represent this relationship, and our chosen model, is Beer-Lambert's law [4]. Denote the surface light intensity at time t and spatial variable x as $\hat{I}(x, t)$, and let b signify a constant denoting the light attenuation factor. Consequently, the available light at time t and depth z can be expressed as

$$I(x, z, t) = \hat{I}(x, t)e^{-b(h-z)}, \quad x \in [0, L] \quad z \in [0, h]. \quad (3.5)$$

3.1.3 Nutrient uptake mechanism

To accumulate biomass, the algae biofilm shall be regularly exposed to adequate nutrients, which are then absorbed through nutrient mass transport. Let us denote $E(x, z, t)$ as the nutrient concentration in the biofilm with spatial element x and depth z at time t with $0 \leq x < L$ and $0 \leq z \leq h$. While the algae biofilm is within the air of the system, $E(x, z, t)$ can be modeled as

$$\partial_t E(x, z, t) = D_E E_{xx} + D E_{zz} - \gamma_a \frac{E(x, z, t)}{K_a + E(x, z, t)} B(x, z, t), \quad x \in [0, L] \quad z \in [0, h] \quad (3.6)$$

where D_E is the diffusion coefficient of the nutrients in the biofilm along the x direction, D is the diffusion coefficient of nutrients in the biofilm in the z direction, K_a is the half-saturation constant, and γ_a is the nutrient consumption rate.

To simplify the model, we assume that the nutrient concentration $E(x, z, t)$ is homogeneous at different depths of the algae biofilm, i.e., E is only a function of x and time. When the algae biofilm is within the water, nutrients are replenished. Therefore, we have the governing equation for the nutrient

$$\partial_t E(x, t) = D_E E_{xx} - \frac{\gamma_{a1} \Gamma(x, t) E(x, t)}{K_a + E(x, t)} \frac{1}{h(x, t)} \int_0^{h(x, t)} B(x, z, t) dz - \gamma_{a2} (1 - \Gamma(x, t)) (E(x, t) - E_T(x, t)), \quad (3.7)$$

where $E_T(x, t)$ is the average nutrient concentration in the water at location x and time t , and γ_{a1}, γ_{a2} control the nutrient uptake and intake rates.

Next, let us consider the finite nature of the nutrients available to the RABR. When the RABR is within the water, nutrients are taken from the water into the algae biofilm. The uptake rate is a function of the current mass of algae biofilm and the proportion of algae biofilm converting itself into algae biomass in the B state. Let $E_T(x, t)$ denote the averaged nutrient concentration in the water at time t . In this context, the nutrient could be phosphorous or ammonia [12]. Therefore, we propose the governing equation for E_T as

$$\partial_t E_T(x, t) = \gamma_T \rho Sh (1 - \Gamma(x, t)) (E(x, t) - E_T(x, t)), \quad (3.8)$$

where γ_T is the effective nutrient consumption rate for the system.

3.1.4 Water evaporation mechanism

We introduce $W(x, t)$ as the water saturation percentage. In the water, $W(x, t) = 1$, and outside of the water, $W(x, t)$ is a monotone decreasing function of time. The governing equation for $W(x, t)$ is proposed as follows

$$\partial_t W(x, t) = D_W W_{xx} - \gamma_{w1} \Gamma(x, t) \frac{W(x, t)}{K_W + W(x, t)} - \gamma_{w2} (1 - \Gamma(x, t)) (W(x, t) - 1), \quad (3.9)$$

where D_w is the diffusion coefficient of water saturation along the x direction of the biofilm, γ_{w1} is the water evaporation rate and γ_{w2} is the absorbing rate from the wastewater.

3.1.5 Biofilm thickness

Next, we consider the thickness of the biofilm and its effect on light attenuation. We denote the algae biomass concentration as $X(x, t)$ with units g/m^2 . We propose the algae growth rate to

be determined by the following equation [4]

$$\partial_t X(x, t) = \left[\frac{1}{h(x, t)} \int_0^{h(x, t)} \mu(x, z, t) dz \right] X(x, t), \quad (3.10)$$

where $h(x, t)$ is the thickness of the biomass, and $\mu(x, z, t)$ is the net growth rate proposed as

$$\mu(x, z, t) = k \frac{B(x, z, t)}{\tau} - R(x, z, t), \quad (3.11)$$

based on the photosynthetic mechanism as shown in Figure 3.1 with $R(x, z, t)$ the respiration rate and k a constant to scale the growth rate. We remark that k shall be determined with empirical studies of algae biofilm growth rates in laboratory settings. We assume $R(x, z, t) = R$ is a constant for simplicity.

Due to the thin nature of biofilm and to reduce the model complexity, we assume that the density of the algae biomass is uniform. This isotropic biofilm is assigned a density ρ , representing the algae biofilm's areal dry biomass density. Therefore, we can represent $X(t)$ as

$$X(x, t) = \rho h(x, t), \quad (3.12)$$

with $h(x, t)$ the height of the biofilm. Substituting (3.11) and (3.12) into (3.10), we obtain

$$\partial_t h(x, t) = \int_0^{h(x, t)} k \frac{B(x, z, t)}{\tau} dz - Rh(x, t). \quad (3.13)$$

Adding the effects of spatial diffusion, nutrient limitation, and the constraints due to water evaporation, we finally obtain the complete version equation for algae biofilm growth as

$$\partial_t h(x, t) = D_h h_{xx} + \int_0^{h(x, t)} k \frac{B(x, z, t)}{\tau} \frac{E(x, t)}{K_a + E(x, t)} \frac{\frac{3}{2}W(x, t)}{K_W + W(x, t)} dz - \left(R + R_W \frac{K_W}{W(x, t) + K_W} \right) h(x, t), \quad (3.14)$$

where D_h is the diffusion coefficient of biofilm height along the x direction of the biofilm, and K_W is the critical water stress threshold for algae biofilm growth. The term $\frac{W(x, t)}{K_W + W(x, t)}$ represents the water stress on algal biofilm growth at location x , and $\frac{K_W}{W(x, t) + K_W}$ represents the water stress on algal biofilm death, R_W is the extra death rate.

3.1.6 Governing equations

Overall, we summarize the proposed models. When considering variables t and z , we have the following system

$$\left\{ \begin{array}{l} \partial_t h(x, t) = D_h h_{xx} + \int_0^{h(x,t)} k \frac{B(x, z, t)}{\tau} \frac{E(x, t)}{K_a + E(x, t)} \frac{\frac{3}{2} W(x, t)}{K_W + W(x, t)} dz - \left(R + R_W \frac{K_W}{W(x, t) + K_W} \right) h(x, t), \\ \partial_t B(x, z, t) = D_B B_{xx} + \sigma I(x, z, t) - \sigma I(x, z, t) C(x, z, t) - \left(\sigma I(x, z, t) + k_d \sigma I(x, z, t) + \frac{1}{\tau} \right) B(x, z, t), \\ \partial_t C(x, z, t) = D_C C_{xx} - k_r C(x, z, t) + k_d \sigma I(x, z, t) B(x, z, t), \\ \partial_t E(x, t) = D_E E_{xx} - \gamma_{a1} \Gamma(x, t) \frac{E(x, t)}{K_a + E(x, t)} \frac{1}{h} \int_0^{h(x,t)} B(x, z, t) dz - \gamma_{a2} (1 - \Gamma(x, t)) (E(x, t) - E_T), \\ \frac{dE_T(t)}{dt} = \frac{1}{VL} \int_0^L \gamma_T S h(x, t) (1 - \Gamma(x, t)) (E(x, t) - E_T) dx, \\ \partial_t W(x, t) = D_W W_{xx} - \gamma_{w1} \Gamma(x, t) \frac{W(x, t)}{K_W + W(x, t)} - \gamma_{w2} (1 - \Gamma(x, t)) (W(x, t) - 1), \end{array} \right. \quad (3.15)$$

where $x \in [0, L]$ and $z \in [0, h(x, t)]$. To better present the parameter choices, we summarize all our model parameters in three tables, representing three types of model parameters. First of all, some model parameters can be fixed based on existing literature [4, 19, 7, 18, 21]. These parameters are summarized in Table 3.1.

Table 3.1: Parameter table with fixed parameter values.

Symbol	Value	Units	Description
σ	1.9×10^{-3}	$m^2 \mu mol^{-1}$	effective absorption rate
t_0	0	s	start of time period of simulated biofilm growth
τ	6.849	s	turnover time of the electron transport chain
k_d	2.99×10^{-4}	s^{-1}	damage rate
k_r	4.8×10^{-4}	s^{-1}	repair rate
R	0.12	d^{-1}	respiration rate
b	1400	m^{-1}	light attenuation factor
ρ	140000	gm^{-3}	dry algae biomass density
p	6	-	number of simulated layers of algal biofilms
C_0	0.2	-	initial value for C state
K_W	0.5	-	critical threshold for water stress
γ_{w1}	2.5×10^{-3}	s^{-1}	rate of evaporation
γ_{w2}	1	s^{-1}	rate of water absorption
γ_{a2}	1	s^{-1}	rate of nutrient absorption
R_W	0.12	d^{-1}	water stress on algal biofilm death
D_A	10^{-6}	$m^2 s^{-1}$	diffusion constant of A amongst spatial element x
D_B	10^{-6}	$m^2 s^{-1}$	diffusion constant of B amongst spatial element x
D_h	10^{-6}	$m^2 s^{-1}$	diffusion constant of h amongst spatial element x
D_E	10^{-5}	$m^2 s^{-1}$	diffusion constant of E amongst spatial element x
D_W	10^{-4}	$m^2 s^{-1}$	diffusion constant of W amongst spatial element x

Secondly, some parameters are based on realistic design parameters. These are summarized

in Table 3.2.

Table 3.2: Parameter table with experimental parameter values.

Symbol	Value	Units	Description
S	1	m^2	surface area of the substratum on the RABR
h_0	0.0005	m	initial height of biofilm
L	7	m	circumference of the substratum on the RABR
l^*	4	m	arc length of the RABR exposed to air
v	0.1555	ms^{-1}	peripheral velocity of the RABR
T	45	s	period of the RABR's rotation
V	50	L	volume of the tank of the RABR
k	0.0001	-	growth rate
γ_{a1}	1575	$\text{mgL}^{-1}\text{d}^{-1}$	rate of the biofilm nutrient consumption
γ_{T}	1.54×10^9	d^{-1}	rate of the total nutrient depletion
K_{a}	1	mgL^{-1}	half-saturation constant for nutrient

We provide the following elaboration on the decisions for some of the parameters found in Table 3.2. The volume V has been selected such that the volume-to-surface area ratio between the RABR media and substratum be 50:1. k has been chosen as 0.0001 such that the resultant productivity values reflect those in existing literature [10]. γ_{a} has been selected such that the biofilm will experience inhibition in growth if not replenished within approximately 8 hours. γ_{T} has been chosen such that in laboratory conditions, the nutrient concentration of the media within the system will be below K_{a} after 72 hours [21].

In addition, parameters with undetermined values are summarized in Table 3.3. Their values will be specified in the corresponding numerical examples.

Table 3.3: Parameter table with undetermined parameter values.

Symbol	Units	Description
$\hat{I}(t)$	$\mu\text{molm}^{-2}\text{s}^{-1}$	light intensity
v	ms^{-1}	peripheral velocity of the RABR
E_0	mgL^{-1}	initial nutrient concentration within the biofilm
$E_{\text{T}0}$	mg	initial nutrient content in the 50-liter system
$h_{\text{harvest}}(x)$	m	height of biofilm to be removed each harvest
t_{harvest}	s	time lags between consecutive biofilm harvests
t_{total}	s	total duration of time within simulation

3.1.7 Harvesting mechanism

As the biofilm grows to more considerable heights, the depth of the biofilm will prevent algae on the bottom layers from receiving sufficient light, eventually leading to a stagnation of growth. To mitigate this stagnation and to maximize productivity, regular harvesting of the algae biofilm occurs in both laboratory and industrial settings to reduce the biofilm height.

Within the context of algae biofilm harvesting, there are two primary parameters to study. The first is the harvesting frequency, labeled as ν_{harvest} ; the second is the residual height of harvesting, labeled as h_{harvest} . When performing a harvest, no harvest will occur if the biofilm height is less than h_{harvest} . Similar arguments apply to the residual height. Intuitively, biofilm harvested too infrequently will experience light-limited stagnation, and biofilm harvested too often will not experience log growth.

Additionally, when harvesting the algae biofilm, consideration must be made of how much algae biofilm to remove. When h_{harvest} is large, much of the algae biofilm will remain after a harvest, implying harvesting will often occur to maintain a certain biofilm height. When h_{harvest} is small, a harvest will remove most of the algae biofilm and imply fewer, more extreme harvests.

To explore the spatial heterogeneity of the numerical model, we will apply several heterogeneous harvesting strategies along the spatial variable x . The methods explored within this paper are listed below:

- Uniform harvest strategy. At the time of harvest, all biofilm along x will be harvested such that $h(x) = h_{\text{harvest}}$ for all x .
- Checker harvest strategy. Suppose the substratum length L is divided into N uniform meshes. Let $j = 0, 1, \dots, N - 1$. If $x_j \bmod 2 = 0$, $h(x_j) = h_{\text{harvest}}$ and if $x_j \bmod 2 = 1$, no biomass shall be removed.
- Linear harvesting strategy. When $j = 0$, $h(x_j) = h_{\text{harvest}}$. When $j = N - 1$, no biomass is removed. For $0 < j < N - 1$, a linear interpolation is used to determine biomass removal.
- Quadratic harvesting strategy. For $j = \frac{N-1}{2}$, no biomass shall be removed. For $j = 0$ and $j = N - 1$, $h(x_j) = h_{\text{harvest}}$. Between $j = 0$ and $j = \frac{N-1}{2}$ and $j = \frac{N-1}{2}$ and $j = N - 1$, a quadratic interpolation is used to determine the biomass removal.

For the aid of visualization, the following schematic of the discussed harvesting strategies is presented in Figure 3.3.

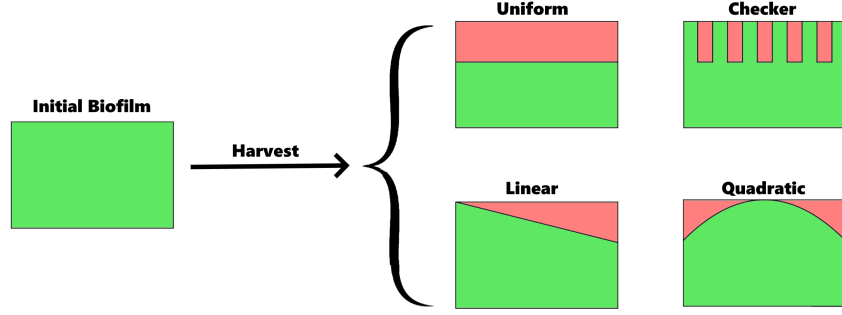


Figure 3.3: A schematic illustration of the harvesting strategies explored within this paper. The areas shaded in red represent the mass that will be removed following the corresponding harvest strategy. The minimum height that will be considered for removal during a harvest is set with h_{harvest} .

3.1.8 Numerical methods

The mathematics model proposed in (3.15) is a free surface problem. It is a coupled system with integral differential equations. To solve (3.15) numerically, we discretize the spatial domain $x \in [0, L]$. We can discretize it into uniform meshes $0 \leq x_0 < x_1 < x_2 < \dots < x_{N-1} \leq L$, where $x_j = (j + 0.5)\Delta$ with $\Delta = \frac{L}{N}$, $j = 0, 1, \dots, N - 1$. Next, we partition the algae biofilm depth domain $[0, h(x_j, t)]$ into p intervals: $0 \leq z_1(x_j, t) < z_2(x_j, t) < \dots < z_p(x_j, t) < h(x_j, t)$ with $z_i(x_j, t) = \frac{i-1}{p}h(x_j, t)$. Notice that when $N = 1$, the model has the same form as that from [22]. Then, by approximating the dynamics with p layers and N segments, we obtain the following system of differential equations to represent the dynamics in each layer and each section:

$$\left\{ \begin{array}{l} \frac{d}{dt} h_j = D_h N^2 \frac{h_{j+1} - 2h_j + h_{j-1}}{L^2} + \sum_{i=1}^p \frac{h_j}{p} k \frac{B_{ij}}{\tau} \frac{E_j}{K_a + E_j} \frac{\frac{3}{2}W_j}{K_W + W_j} - \left(R + R_W \frac{K_W}{W_j + K_W} \right) h_j, \\ \frac{d}{dt} B_{ij} = D_B N^2 \frac{B_{i,j+1} - 2B_{ij} + B_{i,j-1}}{L^2} + \sigma \hat{I}_{ij}(t) - \sigma \hat{I}_{ij}(t) C_{ij} - \left(\sigma \hat{I}_{ij}(t) + k_d \sigma \hat{I}_{ij}(t) + \frac{1}{\tau} \right) B_{ij}, \\ \frac{d}{dt} C_{ij} = D_C N^2 \frac{C_{i,j+1} - 2C_{ij} + C_{i,j-1}}{L^2} - k_r C_{ij} + k_d \sigma \hat{I}_{ij}(t) B_{ij}, \\ \frac{d}{dt} E_j = D_E N^2 \frac{E_{j+1} - 2E_j + E_{j-1}}{L^2} - \gamma_{a1} \Gamma(t) \frac{E_j}{K_a + E_j} \frac{1}{p} \sum_{i=1}^p B_{ij} - \gamma_{a2} (1 - \Gamma_j) (E_j - E_T), \\ \frac{d}{dt} E_T = \frac{L}{VN} \sum_{j=0}^{N-1} \gamma_T \rho S h(x_j, t) (1 - \Gamma_j) (E_j - E_T), \\ \frac{d}{dt} W_j = D_W N^2 \frac{W_{j+1} - 2W_j + W_{j-1}}{L^2} - \gamma_{w1} \Gamma_j \frac{W_j}{K_W + W_j} - \gamma_{w2} (1 - \Gamma_j) (W_j - 1), \end{array} \right. \quad (3.16)$$

where $i = 1, 2, \dots, p$ and $j = 1, 2, \dots, N - 1$. In (3.16), $B_{ij}(t)$ and $C_{ij}(t)$ represent the value at (z_i, x_j) , and the light intensity at the i th layer and j th section is approximated by

$$\hat{I}_{ij}(t) = \frac{P}{h(x_j, t)} \int_{z_i}^{z_{i+1}} I(x_j, z, t) e^{-b(h(x_j, t) - z(x_j))} dz, \quad i = 1, 2, \dots, p, \quad j = 1, 2, \dots, N - 1.$$

Since the initial state is unknown, we assume $C_0 = 0.2$ for all our numerical simulations. Then, we initialize our values of A , B , and C by $(A_0, B_0, C_0) = \left(\frac{1-C_0}{1+\tau\sigma I}, \frac{\tau\sigma I(1-C_0)}{1+\tau\sigma I}, C_0 \right)$, making it compatible with the steady-state solution of the model in [4].

Then, the semi-discrete system in (3.16) is an ODE system. To numerically solve it, we employ the built-in numerical time-integration solver in the SciPy package from Python. We chose the ‘‘BDF’’ method with a maximum time step of 0.1.

3.2 Results

Seven simulations were conducted to explore the inclusion of empirical PPFd values and the spatial variable x for our model. The parameters used to produce these figures are taken from the parameter tables in the previous section. For all simulations utilizing Figure 3.2, we use $t = 8$ hours for the data at the beginning of the simulation to mimic a start at 8:00 AM for the PPFd.

Biofilm growth in a nutrient-limited environment. First, we simulate a seven-day simulation in a nutrient-limited environment using the light data found in Figure 3.2. The numerical results are summarized in Figure 3.4. The oscillations in biofilm height follow the diurnal cycle of the PPFd light data in Figure 3.2. During the times in Figure 3.2 that correspond to daytime, the PPFd is nonzero and encourages biomass growth. At night, when $\text{PPFD} = 0 \mu\text{molm}^{-2}\text{s}^{-1}$, no biomass growth occurs, and the biofilm dynamics are driven by cell respiration. For $0 < t < 6$ days, the biofilm experiences net growth. By $t = 6$ days, E_T approaches 0mg/L and inhibits biofilm growth. The lack of nutrients within the media inhibits this growth for the remainder of the simulation, reflecting a net decrease of biomass for all values of x from $t = 6$ days to $t = 7$ days.

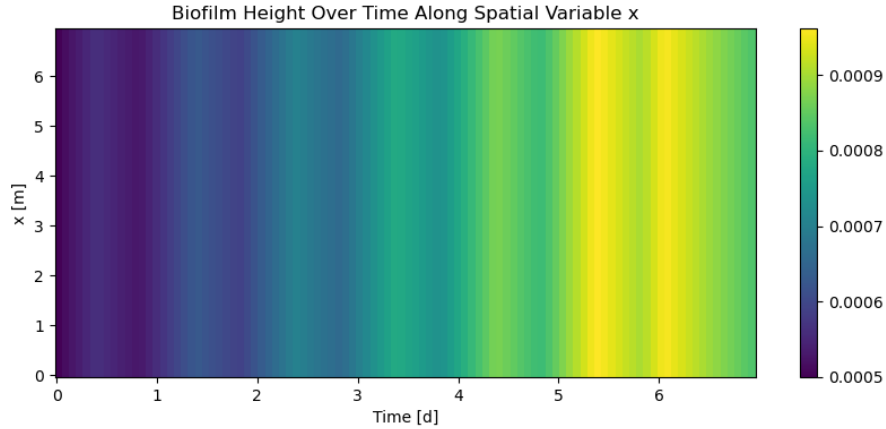


Figure 3.4: This figure displays the biofilm height along the spatial variable x over a seven-day simulation within a nutrient-limited system. At Day 6, E_T approaches 0 and stalls biofilm growth.

Biofilm growth with a RABR deactivation. Next, we perform the following seven-day situation. First, assume the biofilm resides in a nutrient-rich system. Between days 0 and 3, the biofilm resembles that of Figure 3.4 and is homogeneous along the spatial variable x .

Then suppose that on day 3, a mechanical error occurs, and the RABR is deactivated (i.e., $v = 0\text{m/s}$) for 24 hours. During those 24 hours, as $v = 0\text{m/s}$, a proportion of the biofilm along the RABR is fixed within the air regime ($\Gamma(x, t) = 1$), and the remainder is within the water regime ($\Gamma(x, t) = 0$). Recall that from our parameter selection in Table 3.2, 4 meters of the substratum is exposed to the air regime, and 3 meters are exposed to the water regime of the RABR. At $t = 3$ days, $\Gamma(x, t) = 1$ for $6.5 < x < 7$ and $0 < x < 3.5$. During this period in which $v = 0\text{m/s}$, the different mechanisms for biofilm growth and death are exaggerated between the water and air regimes. For the biofilm within the water regime for $t = 3$ days ($3.5 < x < 6.5$), the biofilm experiences zero growth from the lack of PPFD. It slowly diminishes, being driven by cell respiration and metabolism mechanisms. For the biofilm within the air regime for $t = 3$ days ($6.5 < x < 7$ and $0 < x < 3.5$), while the biofilm is exposed to PPFD, over time, the mechanisms of nutrient depletion and water evaporation accelerate the death of the biofilm. Compared to the water regime, the biofilm within the air regime experiences more stress and creates a heterogeneous biofilm along the spatial variable x .

Then, suppose on day 4, the RABR is repaired and rotates appropriately for the remainder of the simulation. Over the remaining days of the simulation, biofilm recovery occurs. Driven by the diffusion terms found in 3.15, the biofilm slowly becomes homogenous along the spatial variable x . By $t = 5$ days, the biofilm is uniform.

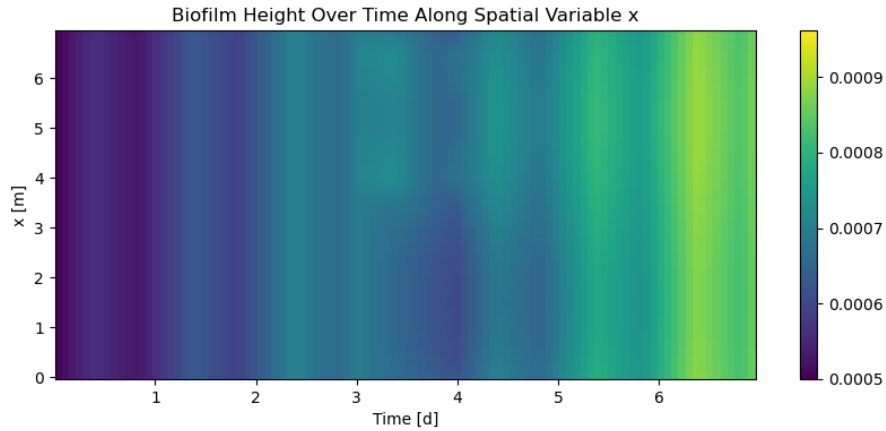


Figure 3.5: This figure displays the biofilm height along the spatial variable x over a seven-day simulation in which $v = 0$ between days 3 and 4. The lack of spinning creates a heterogeneous biofilm and recovers into a more homogeneous structure after day 4.

Impact of the harvesting patterns on biomass productivity. We will now explore the effects of non-homogeneous harvesting strategies on the height and productivity of biofilm. We will explore five strategies: no harvesting, uniform harvesting, checker harvesting, linear harvesting, and quadratic harvesting. The details for the harvesting strategies are found in the previous section. Figure 3.6 shows the results of no harvesting on the biofilm, similar to those discussed in Figure 3.4. This is shown as a control.

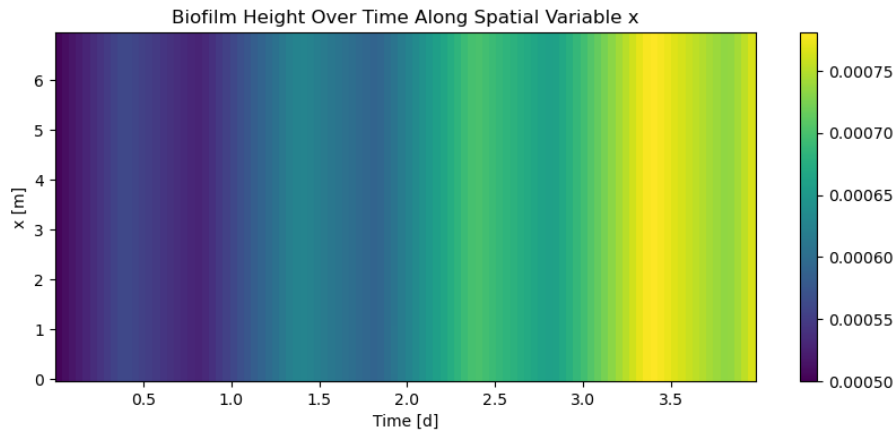


Figure 3.6: This figure displays the biofilm height along the spatial variable x over a four-day simulation. The biofilm resides in a nutrient-rich system, and no harvesting occurs. This is shown as a control compared to the results in Figure 3.7.

The numerical results with various harvesting strategies are summarized in Figure 3.7, with a harvest occurring at $t = 2$ days and using a value of $h_{\text{harvest}} = 0.005 = h_0$. For $0 < t < 2$ days, the biofilm heights within all subfigures of Figure 3.6 and that of Figure 3.6 are identical. After

performing a harvest at $t = 2$ days, the biofilm becomes heterogeneous along the spatial variable x for the checker, linear, and quadratic harvesting strategies. Within 24 hours of the simulation, the biofilms from each harvesting strategy become homogenous along x . Of these strategies, the biofilm following the checker harvest strategy becomes homogeneous the quickest, followed by the quadratic harvest and linear harvest.

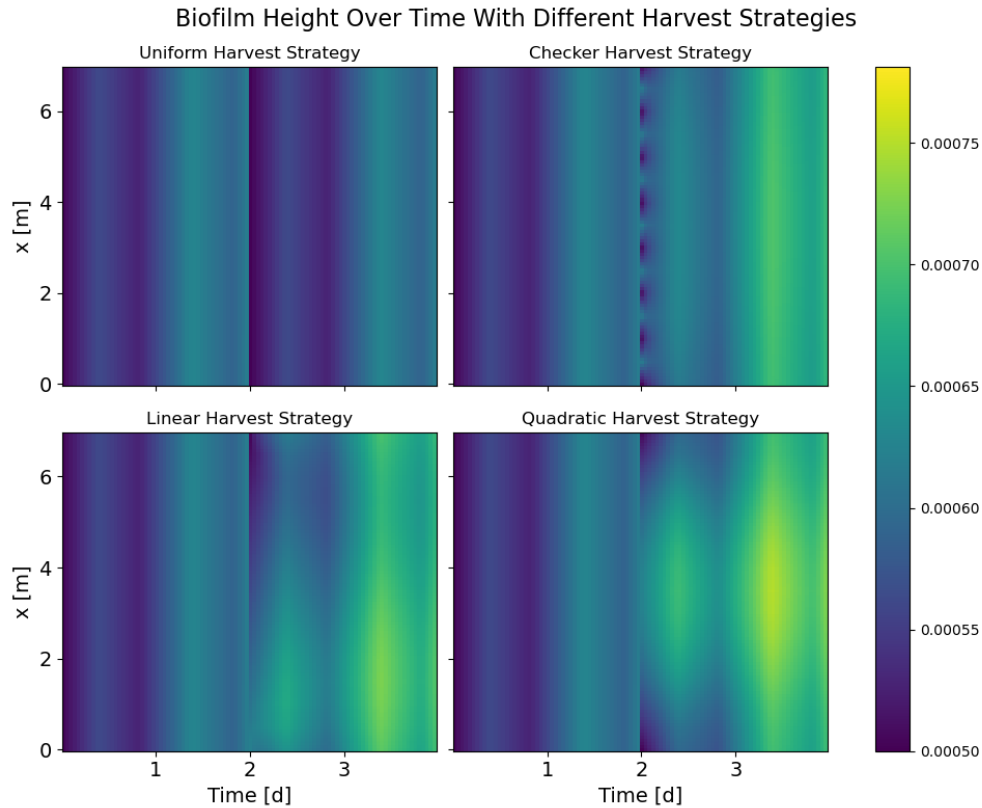


Figure 3.7: This figure compares four harvesting strategies for a RABR over four-day simulations. At $t = 2$ days, a harvest is performed in each simulation. A different harvesting strategy is used in each subfigure in which $h_{\text{harvest}} = 0.0005$. See Methods for details on each harvesting strategy.

For a more thorough comparison of the strategies, the resultant productivity at $t = 4$ days for Figures 3.6 and 3.7 are shown in Table 3.4:

Table 3.4: Final productivity values of selected harvest strategies.

Strategy	Productivity $g/m^2 d$
No Harvest	9.6067
Uniform Harvest	8.6344
Checker Harvest	9.0981
Linear Harvest	9.1302
Quadratic Harvest	9.2451

When analyzing the results of Table 3.4, it appears that for the parameters chosen for Figure

3.7, $\nu_{\text{harvest}} = 2$ days is too frequent to be beneficial for biofilm growth. Notice that the strategy that led to the highest algae biofilm productivity was not performing a harvest, having a resultant productivity of $9.6067\text{g}/(\text{m}^2\text{d})$. The more biomass removed at $t = 2$ days, the smaller the resultant productivity from the simulations performed in Figure 3.7. Of the simulations that perform a harvest, the harvesting strategy that removes the least biofilm, the quadratic harvesting strategy, had a resultant productivity of $9.2451\text{g}/(\text{m}^2\text{d})$. The strategy that removed the most biofilm at $t = 2$ days, the uniform harvesting strategy, had a resultant productivity of $8.6344\text{g}/(\text{m}^2\text{d})$.

Influence of harvesting frequency on biomass productivity. Alongside our investigation of harvesting strategies, we also briefly examine the effects of various harvesting frequencies on biomass productivity. We perform four simulations over a 14-day period, selecting different values of ν_{harvest} : 1 day, 2 days, 3 days, and 7 days. For these simulations, we utilize the checker harvesting strategy and set $h_{\text{harvest}} = 0.0005$. The outcomes of these simulations are depicted in Figure 3.8. The simulation outcomes suggest that excessively frequent harvesting may hinder the algae biofilm from achieving greater thickness. These findings imply that a 7-day harvest interval, or possibly longer, could actually promote more robust algae biofilm growth.

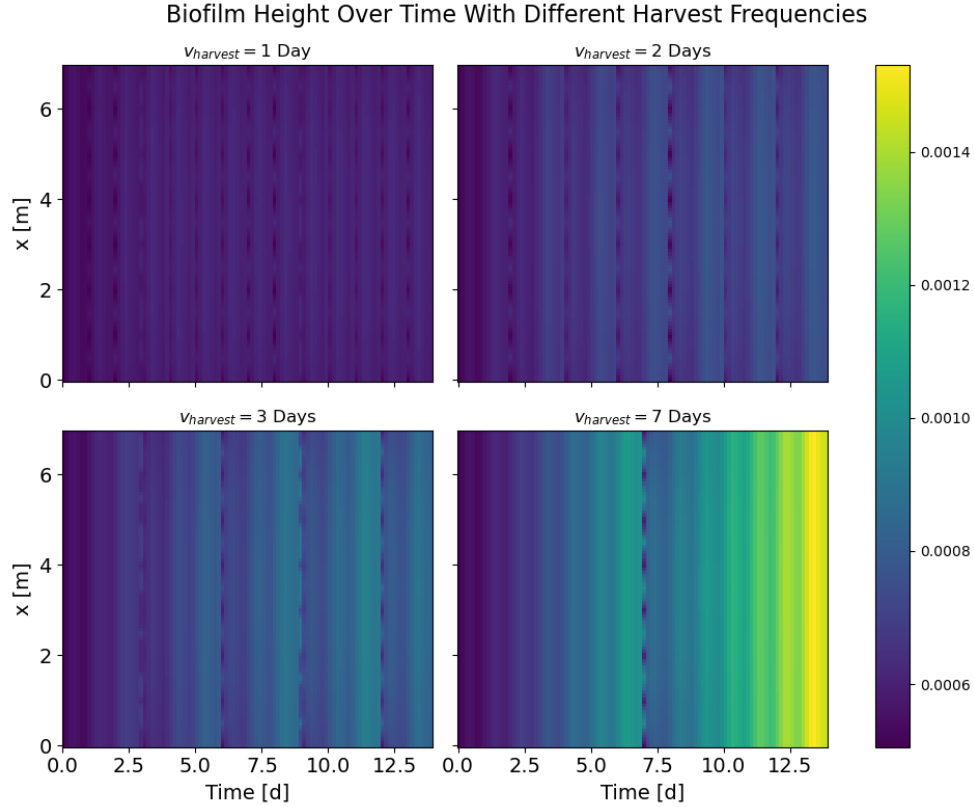


Figure 3.8: This figure presents a comparison of four harvesting frequencies in a RABR over a series of fourteen-day simulations. In each subfigure, the checker harvest strategy is employed, with $h_{\text{harvest}} = 0.0005$. For further details on each harvesting strategy, refer to the previous section.

To facilitate the comparison of different v_{harvest} values, we present the productivity results at $t = 14$ days for Figure 3.8 in Table 3.5. In line with our findings from Table 3.4, the parameters selected for the simulations in Figure 3.8 favor less frequent harvesting approaches. Among the frequencies examined, the least frequent harvests ($v_{\text{harvest}} = 7$ days) yielded the highest productivity at $13.0274\text{g}/(\text{m}^2\text{d})$, while the most frequent harvests ($v_{\text{harvest}} = 1$ day) resulted in the lowest productivity of $8.9354\text{g}/(\text{m}^2\text{d})$.

Table 3.5: Final productivity values of selected harvest frequencies.

v_{harvest}	Productivity $\text{g}/(\text{m}^2\text{d})$
1 day	8.9354
2 days	10.0793
3 days	10.9589
7 days	13.0274

CHAPTER 4

CONCLUSION

We have developed a unified experimental and theoretical framework to investigate the algae biofilm in wastewater treatment on rotating algae biofilm reactors (RABRs). Our unique efforts in joining laboratory experiments and computational mathematical models provide a powerful tool for evaluating and predicting treatment rates of algal nutrients and algae biomass areal productivity utilizing algae biofilm technology at a laboratory scale. The approach combined experimental testing of nutrient and algae biomass changes with mathematical modeling utilizing RABRs. To our best knowledge, this is the first work in the literature to synthesize the algae-based biofilm model with the experimental data generated on a RABR for addressing model parameters. This experimental-theoretical platform could potentially help predict full-scale performance and operations within industrial settings and provide guidance for up-scaled greenhouse and outdoor field testing at a pilot scale site, which is our ongoing research project.

Furthermore, we have taken into account the photosynthetic mechanism and the spatial positioning of the substratum within the reactor. This extension of our model provides a robust surrogate representation of the real-world RABR system. Through our research, we have demonstrated the capabilities of our model in studying the effects of spatial heterogeneity on algae biofilm growth in RABRs, offering valuable insights into the interplay between various factors and their influence on biomass productivity. Our proposed mathematical model with spatial considerations serves as a solid foundation for future studies, facilitating a deeper understanding of the factors governing algae biofilm growth and productivity in the RABR. Furthermore, the spatial capabilities of the model we have developed can be adapted and extended for various applications, including optimizing harvesting strategies and understanding the role of environmental factors in the cultivation of microalgae biofilms. This work contributes significantly to the field, paving the way for more efficient and sustainable RABR systems, ultimately benefiting industries such as bioenergy production, wastewater treatment, and bioproduct development.

Several avenues for future research to further improve and extend the presented model are

being implemented. Our model in Chapter 3 can be extended beyond the 2D case to higher dimensions, allowing for more accurate simulations of real-world RABR systems, which ultimately would require incorporating light data and determining whether the algae are submerged. A more detailed parameter study could be conducted to investigate the optimal time between harvests. This study would help inform practical strategies for algae biofilm reactor management and harvesting strategies. Research can be conducted to study how the hydraulic retention time (HRT) and the rate of nutrient replacement affect algae growth, ultimately leading to improved reactor performance. The developed model in both Chapters 2 and 3 and future improvements can contribute to ongoing efforts at the Central Valley Water Reclamation Facility (CVWRF) to optimize and advance algae-based wastewater treatment technologies.

REFERENCES

- [1] A. Ahmad, S. W. Hassan, and F. Banat. An overview of microalgae biomass as a sustainable aquaculture feed ingredient: food security and circular economy. *Bioengineered*, 13(4):9521–9547, 2022.
- [2] Kanika Arora, Parneet Kaur, Pradeep Kumar, Archana Singh, Sanjay Kumar Singh Patel, Xiangkai Li, Yung-Hun Yang, Shashi Kant Bhatia, and Saurabh Kulshrestha. Valorization of Wastewater Resources Into Biofuel and Value-Added Products Using Microalgal System. *Frontiers in Energy Research*, 9:646571, 2021.
- [3] R. B. Baird and A. D. Eaton. *Standard methods for the examination of water and wastewater*. American Public Health Association (APHA) Press, Washington, DC., 21st edition, 2005.
- [4] Ouassim Bara, Hubert Bonnefond, and Olivier Bernard. Model Development and Light Effect on a Rotating Algal Biofilm. *IFAC-PapersOnLine*, 52(1):376–381, 2019.
- [5] Jay Barlow, Ronald C. Sims, and Jason C. Quinn. Techno-economic and life-cycle assessment of an attached growth algal biorefinery. *Bioresource Technology*, 220:360–368, 2016.
- [6] Quentin Béchet, Andy Shilton, and Benoit Guieysse. Modeling the effects of light and temperature on algae growth: state of the art and critical assessment for productivity prediction during outdoor cultivation. *Biotechnology Advances*, 31(8):1648–1663, 2013.
- [7] Olivier Bernard and Barbara Rémond. Validation of a simple model accounting for light and temperature effect on microalgal growth. *Bioresource technology*, 123:520–527, 2012.
- [8] Bruce E. Chalker. Modeling light saturation curves for photosynthesis: An exponential function. *Journal of Theoretical Biology*, 84(2):205–215, 1980.
- [9] Kit Wayne Chew, Jing Ying Yap, Pau Loke Show, Ng Hui Suan, Joon Ching Juan, Tau Chuan Ling, Duu-Jong Lee, and Jo-Shu Chang. Microalgae biorefinery: High value products perspectives. *Bioresource Technology*, 229:53–62, 2017.

- [10] Logan B Christenson and Ronald C Sims. Rotating algal biofilm reactor and spool harvester for wastewater treatment with biofuels by-products. *Biotechnology and Bioengineering*, 109(7):1674–1684, 2012.
- [11] C. D. Collins and C. W. Boylen. Physiological responses of *Anabaena variabilis* (Cyanophyceae) to instantaneous exposure to various combinations of light intensity and temperature. *Journal of Phycology*, 18(2):206–211, 1982.
- [12] A. Cox, K. Fish, K. Hauck, and C. Miller. Rotating algae bioreactor design for optimization of nutrient uptake and bioproducts, May 2022.
- [13] John J. Cullen. On models of growth and photosynthesis in phytoplankton. *Deep Sea Research Part A. Oceanographic Research Papers*, 37(4):667–683, 1990.
- [14] Metcalf & Eddy and George Tchobanoglous. *Wastewater Engineering: Treatment and Resource Recovery 5th Edition*. McGraw Hill, 5 edition, 2013.
- [15] P. Eilers and J. Peeters. A model for the relationship between light intensity and the rate of photosynthesis in phytoplankton. *Ecological Modelling*, 42(3-4):199–215, 1988.
- [16] W. Francis and M. C. Peters. *Fuels and Fuel Technology: Test methods for petroleum products*. Pergamon, 2nd edition, 1980.
- [17] M. Gross, V. Mascarenhas, and Z. Wen. Evaluating algal growth performance and water use efficiency of pilot-scale revolving algal biofilm (RAB) culture systems. *Biotechnology and Bioengineering*, 112(10):2040–2050, 2015.
- [18] Bo-Ping Han. A mechanistic model of algal photoinhibition induced by photodamage to photosystem-II. *Journal of Theoretical Biology*, 214(4):519–527, 2002.
- [19] Bo-Ping Han, Markku Virtanen, Jorma Koponen, and Milan Straškraba. Effect of photoinhibition on algal photosynthesis: a dynamic model. *Journal of Plankton Research*, 22(5):865–885, 2000.
- [20] Kyle M. Hillman and Ronald C. Sims. Struvite formation associated with the microalgae biofilm matrix of a rotating algal biofilm reactor (RABR) during nutrient removal from municipal wastewater. *Water Science and Technology*, 81(4):644–655, 2020.

- [21] G. Jones, R. Sims, and J. Zhao. Experimental and theoretical investigations of rotating algae biofilm reactors (RABRs): Areal productivity, nutrient recovery, and energy efficiency. *under review for Biotechnology and Bioengineering*, 2023.
- [22] Gerald Jones, Dylan Ellis, Zengyan Zhang, Jia Zhao, and Ronald Sims. Optimizing Algae Biofilm Growth in Wastewater Treatment using Predictive Mathematical Models. In *Contemporary Research in Mathematical Biology*, page 600. World Scientific, 2023.
- [23] Maureen Kesaano and Ronald C Sims. Algal biofilm based technology for wastewater treatment. *Algal Research*, 5:231–240, 2014.
- [24] S. H. Lee, H.-M. Oh, B.-H. Jo, S.-A. Lee, S.-Y. Shin, H.-S. Kim, S.-H. Lee, and C.-Y. Ahn. Higher biomass productivity of microalgae in an attached growth system, using wastewater. *Journal of Microbiology and Biotechnology*, 12(11):1566–1573, 2014.
- [25] T. Liu, J. Wang, Q. Hu, P. Cheng, B. Ji, J. Liu, Y. Chen, W. Zhang, X. Chen, and L. Chen. Attached cultivation technology of microalgae for efficient biomass feedstock production. *Biore-source Technology*, 127:216–222, 2013.
- [26] Martínez-Ruiz M, Martínez-González CA, Kim DH, Santiesteban-Romero B, Reyes-Pardo H, Villaseñor-Zepeda KR and Meléndez-Sánchez ER, Ramírez-Gamboa D, Díaz-Zamorano AL, Sosa-Hernández JE, Coronado-Apodaca KG, Gámez-Méndez AM, Iqbal HMN, and Parra-Saldivar R. Microalgae bioactive compounds to topical applications products-a review. *Molecules*, 27(11):3512, 2022.
- [27] Savvas Giannis Mastropetros, Konstantinos Pispas, Dimitris Zagklis, Sameh S. Ali, and Michael Kornaros. Biopolymers production from microalgae and cyanobacteria cultivated in wastewater: Recent advances. *Biotechnology Advances*, 60:107999, 2022.
- [28] Marjorie Morales, Hubert Bonnefond, and Olivier Bernard. Rotating algal biofilm versus planktonic cultivation: Lca perspective. *Journal of Cleaner Production*, 257:120547, 2020.
- [29] C. Mulder and A. J. Hendricks. Half-saturation constants in functional responses. *Global Ecology and Conservation*, 2, 2014.
- [30] B. Polizzi, O. Bernard, and M. Ribot. A time-space model for the growth of microalgae biofilms for biofuel production. *Journal of Theoretical Biology*, 432:55–79, 2017.

- [31] Bastien Polizzi, Andrea Fanesi, Filipa Lopes, and Magali Ribot and Olivier Bernard. Understanding photosynthetic biofilm productivity and structure through 2d simulation. *PLoS Computational Biology*, 18(4):e1009904, 2022.
- [32] Asif Rahman, Ryan J. Putmana, Kadriye Inan, Fulya Ay Sal, Ashik Sathish, Terence Smith, Chad Nielsen, Ronald C. Sims, and Charles D. Miller. Polyhydroxybutyrate production using a wastewater microalgae based media. *Algal Research*, 8:95–98, 2015.
- [33] E.W. Rice, R.B. Baird, and A.D. Eaton. *Standard Methods for the Examination of Water and wastewater*. American Public Health Association, American Water Works Association, Water Environment Federation, 23 edition, 2022.
- [34] I. Saadaoui, R. Rasheed, A. Aguilar, and et al. Microalgal-based feed: promising alternative feedstocks for livestock and poultry production. *Journal of Animal Science and Biotechnology*, 12(76), 2021.
- [35] P. K. Sharma, M. Saharia, R. Srivastava, S. Kumar, and Sahoo L. Tailoring microalgae for efficient biofuel production. *Frontiers in Marine Science*, 5, 2018.
- [36] R. Sims and B. Peterson. Waste to value: algae-based biofuel utilizing oil and gas extraction wastewater. *Academia Letters*, 4460:12–21, 2021.
- [37] S. Thapa, A. Bharti, and R. Prasanna. Algal biofilms and their biotechnological significance. *Recent Progress in Biotechnology*, pages 285–303, 2017.
- [38] Jonathan L. Wood, Charles D. Miller, Ronald C. Sims, and Jon Y. Takemoto. Biomass and phycocyanin production from cyanobacteria dominated biofilm reactors cultured using oilfield and natural gas extraction produced water. *Algal Research*, 11:165–168, 2015.
- [39] Jonathan L. Wood, Jon Y. Takemoto, and Ronald C. Sims. Rotating Algae Biofilm Reactor for Management and Valorization of Produced Wastewater. *Frontiers in Energy Research*, 10:774760, 2022.
- [40] X. Wu and J. C. Merchuk. A model integrating fluid dynamics in photosynthesis and photoinhibition processes. *Chemical Engineering Sciences*, 56:3527–3538, 2001.
- [41] Siyong Yang, Ashik Sathish, Jong-Su Eun, Young Min Lee, Vivek Fellner, and Ronald C. Sims. In vitro ruminal fermentation characteristics of algal protein precipitate supplemented

in lactation dairy diets in continuous cultures. *International Journal of Innovative Research in Science, Engineering and Technology*, 8(9):9207–9218, 2019.

- [42] S. Zhang, L. Zhang, G. Xu, F. Li, and X. Li. A review on biodiesel production from microalgae: Influencing parameters and recent advanced technologies. *Frontiers in Microbiology*, 12:970028, 2022.

Appendix A
SUPPLEMENTAL MATERIALS FOR CHAPTER 2

A.1 AI procedure/method summary

- Area measurement: Remove 4 cm² of biofilm from the cultivation surface and measure wet weight.
- Ash-free dry weight measurement: Determine dry weight at 105°C and ash content at 550 °C (Muffle Furnace) to determine ash-free dry weight (AFDW) for 4 cm² biofilm area
- Chlorophyll-a extraction of 4cm²: to another biofilm sample add 5 mL acetone/MgCO₃ solution and allow the mixture to react for 10 minutes in the dark (light can degrade chlorophyll) using a motor and pestle; centrifuge samples at 500 rpm to remove solids (cells and other debris) and collect supernatant containing chlorophyll-a.
- Chlorophyll-a concentration: Use a spectrophotometer to read absorbance at wavelengths of 664, 647, 750, and 630 nm and calculate chlorophyll concentration as mg/L using optical density (OD) readings from the spectrometer and the equation:

$$\text{Chl-a(mg/L)} = 11.85(\text{OD}_{664} - \text{OD}_{750}) - 1.54(\text{OD}_{647} - \text{OD}_{750}) - 0.08(\text{OD}_{630} - \text{OD}_{750})$$

Convert Chl-a (mg/L) to (mg/m²) using the equation:

$$\text{Chl-a(mg/m}^2\text{)} = \frac{[(\text{Chl-a}), \text{mg/L}][\text{extract volume, L}]}{[\text{sample area, m}^2]} = \frac{\text{mgChl-a}}{\text{m}^2}$$

- Calculate autotrophic index (AI):

$$\text{AI} = \frac{\text{AFDW biomass per sample area(mg/m}^2\text{)}}{\text{Chlorophyll-a concentration per sample area}} = \frac{\text{AFDW, mg/m}^2}{\text{Chl-a, mg/m}^2}$$

A.2 Bomb calorimeter procedure/method summary

- Weigh 1 g (dry weight) of biofilm sample
- Place the sample in the bomb vessel and seal
- Let 20 atm of oxygen into the bomb
- Place 2 L of water of know temperature into the holding bucket and lower the bomb into the bucket
- Engage the ignition button to combust the sample and measure change in temperature of the water to measure the heat of combustion
- Use the equation to calculate the heat of combustion of the sample and energy per g:

$$q_s = \frac{(C_{\text{cal}})(\Delta K)(J/K)}{m_s(g)} = \frac{J}{g},$$

where C_{cal} denotes heat capacity of the calorimeter, and m_s denotes mass of the sample.

A.3 Defining total power within simulations

To explicitly define the energy demand of the RABR for our simulations (expressed in units kW), we center our calculations on the moment of inertia of a hollow cylinder, the assumed geometry of the RABR. Let I_{RABR} represent the moment of inertia of the RABR. So,

$$I_{\text{RABR}} = \frac{1}{2}M(r_1^2 + r_2^2), \quad (\text{A.1})$$

where M is the mass of the RABR and r_1 and r_2 are the outer and inner radii of the cylinder. Next, recall the relationship between the moment of inertia and rotational energy, defined as E_{RABR} :

$$E_{\text{RABR}} = \frac{1}{2}(I_{\text{RABR}})\omega^2, \quad (\text{A.2})$$

where ω is the angular velocity of the RABR. Then, substituting (A.1) for I_{RABR} and writing ω in terms of peripheral velocity v , we have

$$E_{\text{RABR}} = \frac{1}{2} \left(\frac{1}{2}M(r_1^2 + r_2^2) \right) \left(\frac{2\pi v}{L} \right)^2, \quad (\text{A.3})$$

where L is the circumference of the outer radius of the RABR. Then, as power P is a product of energy and time, the rotational power throughout the simulation, denoted as R_{RABR} , is

$$R_{\text{RABR}} = (E_{\text{RABR}})\delta(t_{\text{total}}), \quad (\text{A.4})$$

where δ is the duty cycle of the RABR and t_{total} is the total duration of the simulation, measured in seconds.

Next, let us define overhead power O . When the RABR is not actively rotating, we assume there exists a small, constant, energy demand on the RABR. To determine this overhead power O , we assume that for every hour passed within our simulation, O is equal to the power required to rotate the RABR once at velocity v . Therefore,

$$O_{\text{RABR}} = E_{\text{RABR}} \left(\frac{L}{v} \right) \left(\frac{t_{\text{total}}}{3600} \right). \quad (\text{A.5})$$

Therefore, when combining (A.4) and (A.5), we have

$$\begin{aligned} P &= R_{\text{RABR}} + O_{\text{RABR}} \\ &= (E_{\text{RABR}})\delta(t_{\text{total}}) + (E_{\text{RABR}}) \frac{L}{v} \frac{t_{\text{total}}}{3600} \\ &= (E_{\text{RABR}})(t_{\text{total}}) \left(\delta + \frac{L}{3600v} \right) \\ &= \frac{t_{\text{total}}}{4} \left(M(r_1^2 + r_2^2) \left(\frac{2\pi v}{L} \right)^2 \right) \left(\delta + \frac{L}{3600v} \right). \end{aligned}$$

A.4 Governing equations

We summarize the proposed models. When considering variables t and z in (2.2), we have the following system

$$\left\{ \begin{array}{l} \frac{dh(t)}{dt} = \int_0^{h(t)} k \frac{B(z,t)}{\tau} \frac{E(t)}{K_a + E(t)} \frac{\frac{3}{2}W(t)}{K_W + W(t)} dz - \left(R + R_W \frac{K_W}{W(t) + K_W} \right) h(t), \\ \frac{\partial B(z,t)}{\partial t} = \sigma I(z,t) - \sigma I(z,t) C(z,t) - \left(\sigma I(z,t) + k_d \sigma I(z,t) + \frac{1}{\tau} \right) B(z,t), z \in [0, h], \\ \frac{\partial C(z,t)}{\partial t} = -k_r C(z,t) + k_d \sigma I(z,t) B(z,t), \quad z \in [0, h], \\ \frac{dE(t)}{dt} = -\gamma_{a1} \Gamma(t) \frac{E(t)}{K_a + E(t)} \frac{1}{h} \int_0^h B(z,t) dz - \gamma_{a2} (1 - \Gamma(t)) (E(t) - E_T), \\ \frac{dE_T}{dt} = \gamma_T \frac{Sh}{V} (1 - \Gamma(t)) (E(t) - E_T), \\ \frac{dW(t)}{dt} = -\gamma_{w1} \Gamma(t) \frac{W(t)}{K_W + W(t)} - \gamma_{w2} (1 - \Gamma(t)) (W(t) - 1). \end{array} \right. \quad (\text{A.6})$$

A.5 Parameters

To better present the parameter choices, we summarize all our model parameters in three tables, representing three types of model parameters. Firstly, some model parameters can be fixed based on existing literature [4, 19, 7, 18] and our best guess that is consistent with our laboratory setups. These parameters are summarized in Table A.1.

Table A.1: Parameter table with fixed parameter values.

Symbol	Value	Units	Description
σ	1.9×10^{-3}	$\text{m}^2 \mu\text{mol}^{-1}$	effective absorption rate
t_0	0	s	start of time period of simulated biofilm growth
τ	6.849	s	turnover time of the electron transport chain
k_d	2.99×10^{-4}	s^{-1}	damage rate
k_r	4.8×10^{-4}	s^{-1}	repair rate
R	0.12	d^{-1}	respiration rate
b	2000	m^{-1}	light attenuation factor
ρ	140000	g m^{-3}	dry algae biomass density
p	10	-	number of simulated layers within the algal biofilm, as selected from the numerical study shown in Figure A.6
h_0	1.0×10^{-4}	m	initial height of biofilm
C_0	0.2	-	initial value for C state
K_W	0.5	-	critical threshold for water stress
γ_{w1}	2.5×10^{-3}	s^{-1}	rate of evaporation
γ_{w2}	1	s^{-1}	rate of water absorption
γ_{a2}	1	s^{-1}	rate of nutrient absorption
R_W	0.12	d^{-1}	water stress on algal biofilm death

Secondly, some parameters are based on our specific experimental setup for collecting the ammonia and phosphorus data [29]. These are summarized in Table A.2. We note here the surface area S is measured from one of the RABRs in Figure 2.1.

Table A.2: Parameter table with experimental parameter values.

Symbol	Value	Units	Description
$\hat{I}(t)$	700 or 0	$\mu\text{molm}^{-2}\text{s}^{-1}$	light intensity
S	0.00770103	m^2	plan view area of the RABR
M	1.5	kg	the mass of the RABR, assumed to be constant for energy calculations
r_1	0.025265	m	outer radius of the hollow cylinder of the RABR
r_2	0.021475	m	inner radius of the hollow cylinder of the RABR, assumed to be 85% the length of r_1 .
L	0.15875	m	circumference of the substratum on the RABR
l^*	0.1	m	arc length of the RABR exposed to air
V	1	L	volume of the media that the RABR is suspended in
v	0.015875	ms^{-1}	peripheral velocity of the RABR
δ	1.0	-	duty cycle of the RABR
δ_p	60	s	duty cycle period of the RABR
T	10	s	period of the RABR's rotation
t_{total}	8	d	elapsed days in simulation
E_0	14.1	mgL^{-1}	initial phosphorus concentration within the biofilm
E_{T_0}	14.1	mgL^{-1}	initial phosphorus content in the 1-liter system
K_a	0.04	mgL^{-1}	half-saturation constant for phosphorus
E_0	283.4	mgL^{-1}	initial ammonia concentration within the biofilm
E_{T_0}	283.4	mgL^{-1}	initial ammonia content in the 1-liter system
K_a	1	mgL^{-1}	half-saturation constant for ammonia

In addition, several free parameters must be determined, summarized in Table A.3. These parameters are fine-tuned to make the model (A.6) agree with our experimental data.

Table A.3: Parameter table with tuned parameter values.

Symbol	Value	Units	Description
k	5×10^{-5}	-	growth rate
γ_{a1}	73	$\text{mgL}^{-1}\text{d}^{-1}$	rate of the biofilm phosphorus consumption
γ_T	1.764×10^{10}	d^{-1}	rate of the total phosphorus depletion
γ_{a1}	1470	$\text{mgL}^{-1}\text{d}^{-1}$	rate of the biofilm ammonia consumption
γ_T	8.47×10^9	d^{-1}	rate of the total ammonia depletion

A.6 Parameter tuning

Table A.2 delineates the parameters used for the model that reflects experimental parameters in [12]. There are a few considerations in determining this table. We assume a uniform PPFd value in the simulation since we make no distinction between the nutrient data collected when PPFd=700 $\mu\text{mol}/(\text{m}^2\text{s})$ versus PPFd=1000 $\mu\text{mol}/(\text{m}^2\text{s})$. Specifically, we let PPFd=700 $\mu\text{mol}/(\text{m}^2\text{s})$ when the light is present in the simulated diurnal cycle. Additionally, we ignore the effects of the duty cycle and do not incorporate them into the model. So, for simplicity, we assume our simulated RABR is continuously spinning. Therefore, five parameters remain to be tuned to best fit the empirical results of the experiments, which are summarized in Table A.3.

Growth rate k. First, we want to get a growth rate based on the experimental data. We want the areal productivity of the model to be similar to the values we see in experiments. Setting all the parameters found in Table A.1 and Table A.2, we then let $\gamma_{a1} = \gamma_{a2} = 0$ and $\gamma_T = 0$ to ignore nutrient depletion effects on the system. Then using the numerical steps found in the previous section and $t_{\text{total}} = 12$ days and recording every 60 minutes, we get the following results for the parameter study k in Figure 2.4.

Biofilm nutrient consumption rate γ_{a1} . The selection of γ_{a1} was derived as follows. First, we initialize $\Gamma = 0$ to simulate the RABR not being in contact with the nutrients in the tank. Then, the velocity of the RABR was set to 0 to ensure no nutrient replenishment occurred. Then, using all the same parameters shown in Table A.1 and Table A.2 and $k = 5 \times 10^{-5}$, we tune γ_{a1} such that after approximately 8 hours, the values of E are less than their respective Michaelis Menten constant for that nutrients.

Total nutrient depletion rate γ_T . Following the selection of k and the appropriate values for γ_{a1} , we now tune γ_T in (A.6) to fit better the nutrient depletion data collected in previous sections. The ideal value of γ_T for ammonia is $8.47 \times 10^9 \text{ gm}^{-1} \text{ d}^{-1}$ and $\gamma_T = 1.764 \times 10^{10} \text{ gm}^{-1} \text{ d}^{-1}$ for phosphorus. The fit of these parameter values is shown in Figure 2.6.

A.7 Numerical methods

The mathematics model proposed in (A.6) is a free surface problem. It is a coupled system with integral differential equations. In order to solve (A.6) numerically, we discretize the spatial domain $[0, h(t)]$ into p intervals: $0 \leq z_1(t) < z_2(t) < \dots < z_p(t) < h(t)$ with $z_i(t) = \frac{i-1}{p}h(t)$. The bottom position of each i th layer is used to represent z_i to best penalize tall biofilm heights. Alternatively, one can choose the midpoint of the layer. By approximating the dynamics with p layers, we obtain the following system of differential equations to represent the dynamics in each layer:

$$\frac{d}{dt}h(t) = \sum_{i=1}^p \frac{h(t)}{p} k \frac{B_i}{\tau} \frac{E(t)}{K_a + E(t)} \frac{\frac{3}{2}W(t)}{K_W + W(t)} - \left(R + R_W \frac{K_W}{W(t) + K_W} \right) h(t), \quad (\text{A.7})$$

$$\frac{d}{dt}B_i = \sigma \hat{I}_i(t) - \sigma \hat{I}_i(t) C_i - \left(\sigma \hat{I}_i(t) + k_d \sigma \hat{I}_i(t) + \frac{1}{\tau} \right) B_i, \quad z \in [0, h], \quad i = 1, 2, \dots, p, \quad (\text{A.8})$$

$$\frac{d}{dt}C_i = -k_r C_i + k_d \sigma \hat{I}_i(t) B_i, \quad z \in [0, h], \quad i = 1, 2, \dots, p, \quad (\text{A.9})$$

$$\frac{d}{dt}E(t) = -\gamma_{a1} \Gamma(t) \frac{E(t)}{K_a + E(t)} \frac{1}{p} \sum_{i=1}^p B_i - \gamma_{a2} \left(1 - \Gamma(t) \right) (E(t) - E_T), \quad (\text{A.10})$$

$$\frac{d}{dt}E_T = \gamma_T \frac{Sh}{V} (1 - \Gamma(t)) (E(t) - E_T), \quad (\text{A.11})$$

$$\frac{d}{dt}W(t) = -\gamma_{w1} \Gamma(t) \frac{W(t)}{K_W + W(t)} - \gamma_{w2} \left(1 - \Gamma(t) \right) (W(t) - 1), \quad (\text{A.12})$$

where $B_i(t)$ and $C_i(t)$ represent the value at $z = z_i(t)$, and the light intensity at the i th layer is approximated by

$$\hat{I}_i(t) = \frac{p}{h} \int_{z_i}^{z_{i+1}} I(z, t) e^{-b(h(t)-z)} dz, \quad i = 1, 2, \dots, p.$$

We remark that we use the assumption that $C_0 = 0.2$ for all of our numerical simulations in this chapter. Also, in the rest of this chapter, we initialize our values of A , B , and C by

$$(A_0, B_0, C_0) = \left(\frac{1 - C_0}{1 + \tau \sigma I}, \frac{\tau \sigma I (1 - C_0)}{1 + \tau \sigma I}, C_0 \right),$$

For our numerical calculations. This is compatible with the steady-state solution for the model in [4].

Then, the semi-discrete system in (A.7) is an ODE system. We introduce the notation

$$\Phi(t) = [h(t) \ B_1(t) \ B_2(t) \ \dots \ B_p(t) \ C_1(t) \ C_2(t) \ \dots \ C_p(t) \ E(t) \ W(t) \ E_T(t)]^T, \quad (\text{A.13})$$

and denote the ODE system in (3.16) as

$$\begin{cases} \frac{d}{dt} \Phi(t) = F(\Phi(t)), \\ \Phi(0) = \Phi_0, \end{cases} \quad (\text{A.14})$$

with F the reactive kinetics. To numerically solve the system in (A.14), we employ the built-in numerical time-integration solver in the SciPy package from Python. We chose the "BDF" method with a maximum time step of 0.1.

A.8 Supplemental figures

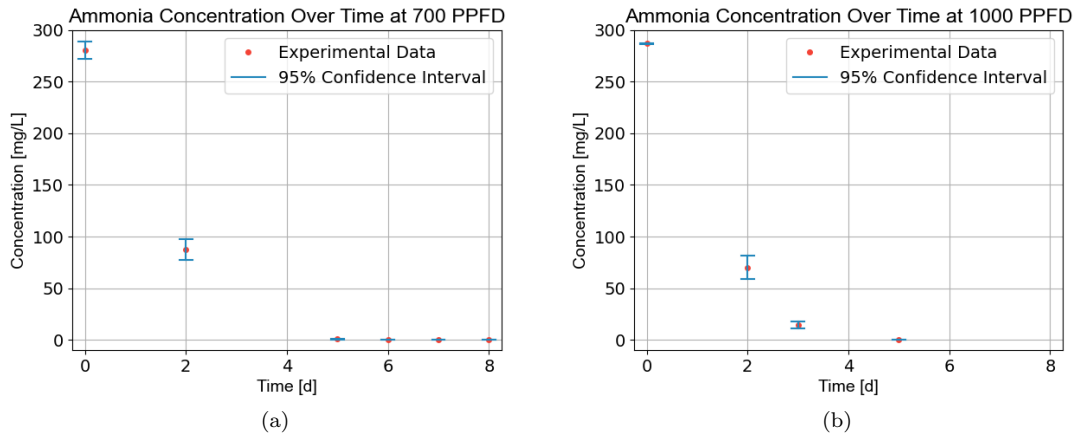


Figure A.1: Ammonia data from Figure 2.5 grouped by their relative time since the most recent influent replacement. Figure (a) visualizes the data for all sampling with $700\mu\text{mol}/(\text{m}^2\text{s})$, and (b) shows the data with $1000\mu\text{mol}/(\text{m}^2\text{s})$. The concentration is measured by mg/L .

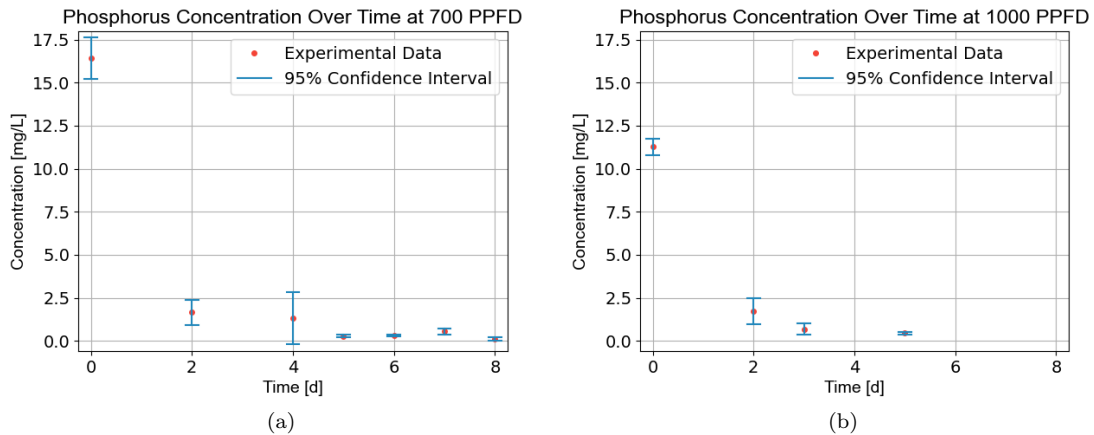


Figure A.2: All phosphorus data grouped by epochs of influent replacement. The red dot is the average for that day, and the blue lines are the 95% confidence intervals. The concentration is measured by mg/L .

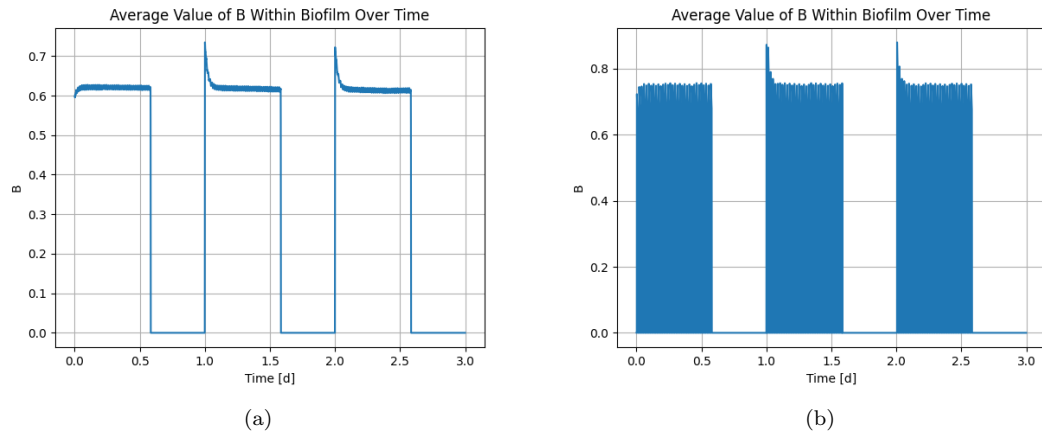


Figure A.3: The average value of the activated state (B state) of all algae biofilm layers over time, measured every minute, and a total time of 3 days. In (a), we use 375 RPM, and in (b), we use 0.0375 RPM. The gaps of time in which the activated state (B) equals $= 0$ correspond to when $\text{PPFD} = 0 \mu\text{mol}/(\text{m}^2\text{s})$ to mimic the diurnal cycle described in Section 2. The parameters used to produce these figures are taken from the parameter tables A.1, A.2 and A.3.

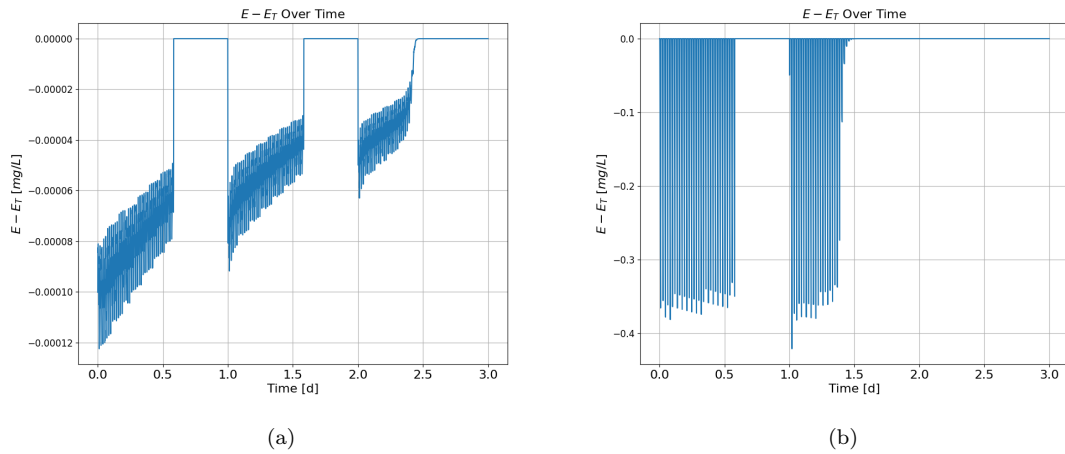


Figure A.4: The value of $(E(t) - E_T(t))$ over time, measured every 60 seconds and a total time of 3 days. In (a), we use 375 RPM, and in (b) we use 0.0375 RPM. The gaps of time in which $E - E_T = 0$ correspond to when $\text{PPFD} = 0 \mu\text{mol}/(\text{m}^2\text{s})$ to mimic the diurnal cycle described in Section 2. The rest parameters used to produce these results are taken from parameters tables A.1, A.2 and A.3.

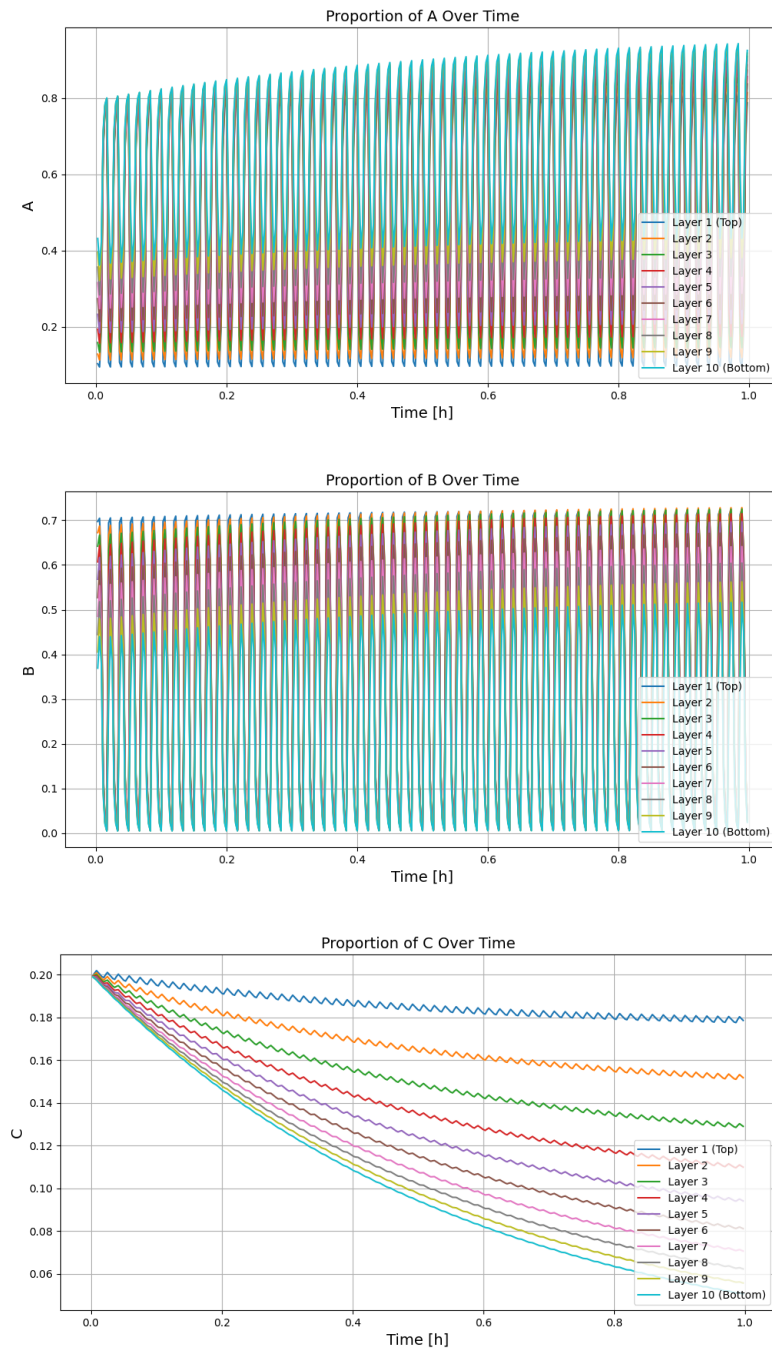


Figure A.5: This figure displays the values of A, B, and C for all 10 layers in a simulation of 30 minutes with $p = 10$. All parameters used in the simulation are the same as those used to generate the surface plots presented in Section 3, with the exception of the PPF, which was held constant at 700, and a RABR peripheral velocity of 1 RPM.

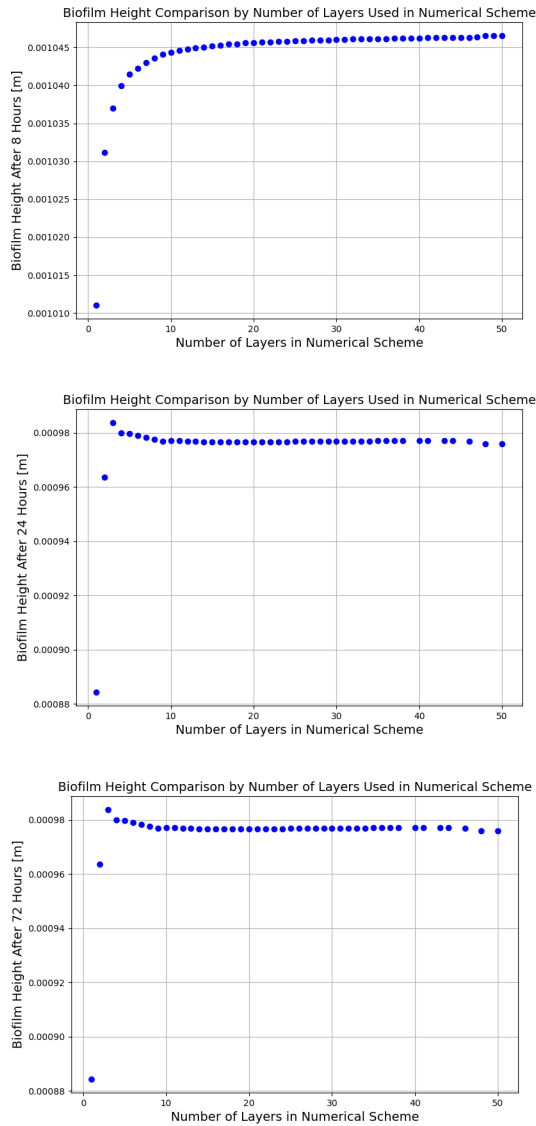


Figure A.6: This figure illustrates a parameter study of the number of layers in the numerical scheme, using the same parameters as those selected in Figure 2.6, with the exception of the PPF_D, which was held constant at 700, and a RABR peripheral velocity of 1 RPM. Panel (a) shows the results at 8 hours, panel (b) at 1 day, and panel (c) at 72 hours. As the number of discretized layers in the numerical scheme decreases, the biofilm height is underestimated.

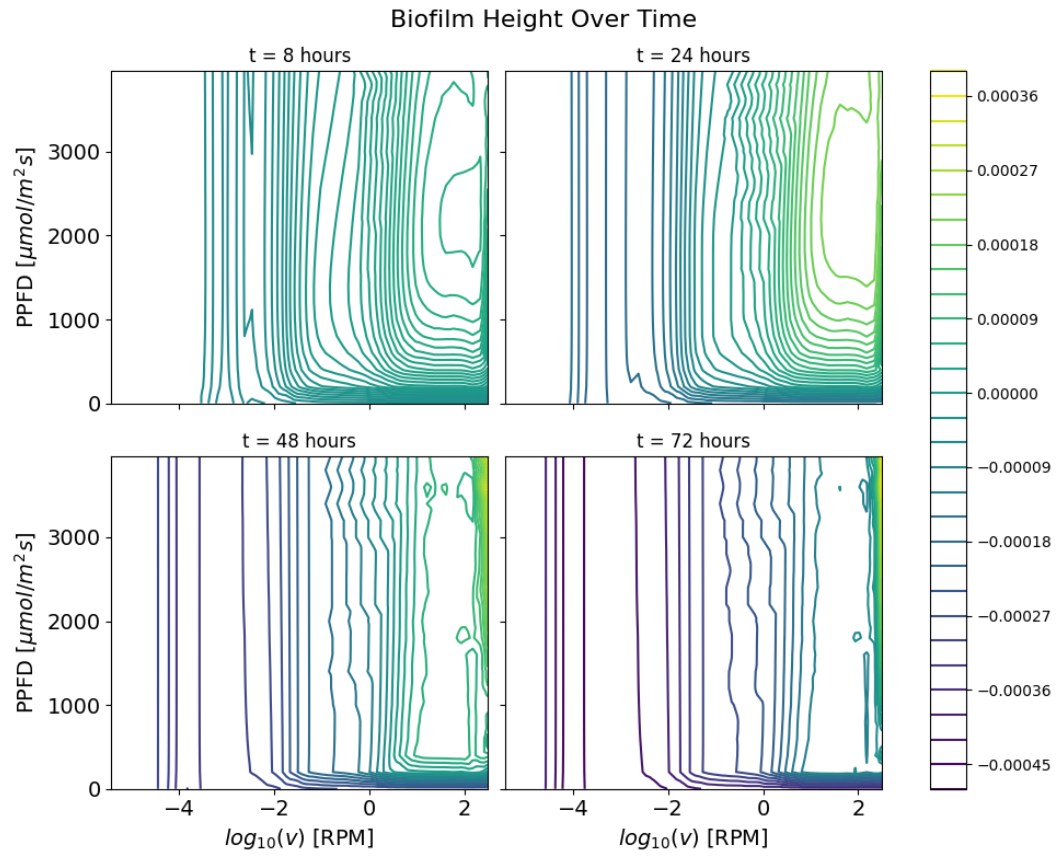


Figure A.7: This figure displays the contour plots to supplement the results in Figure 2.7.

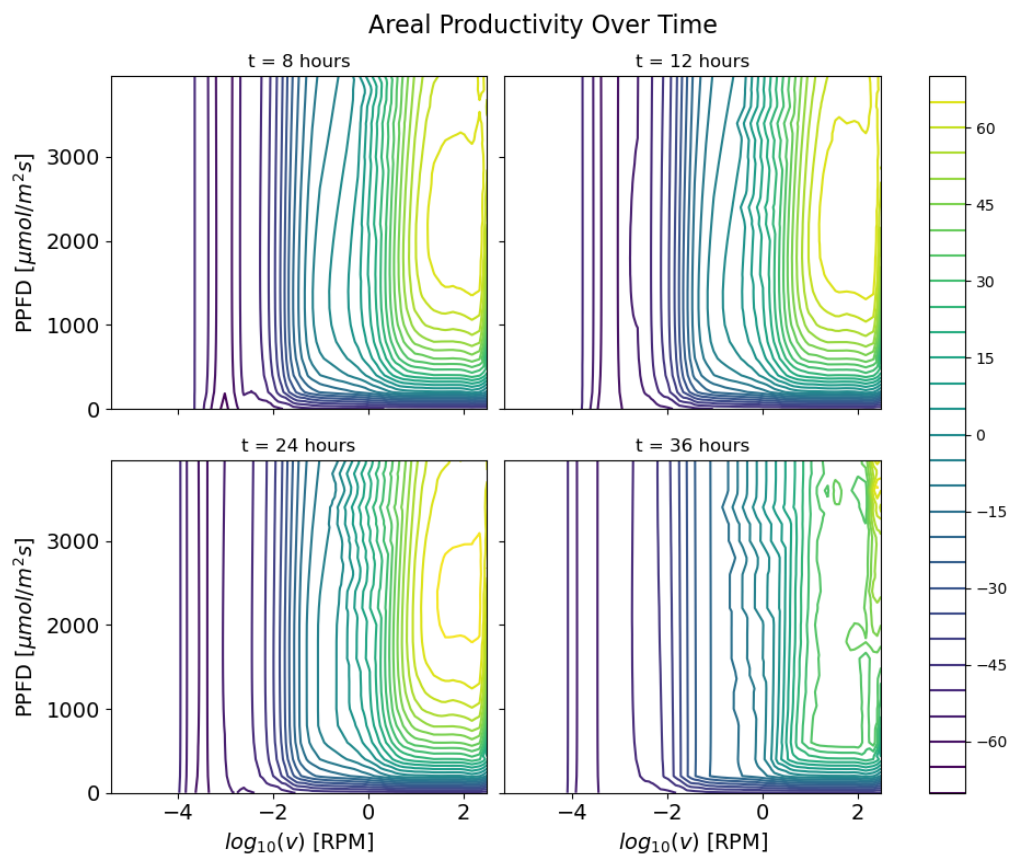


Figure A.8: This figure displays the contour plots to supplement the results in Figure 2.8.

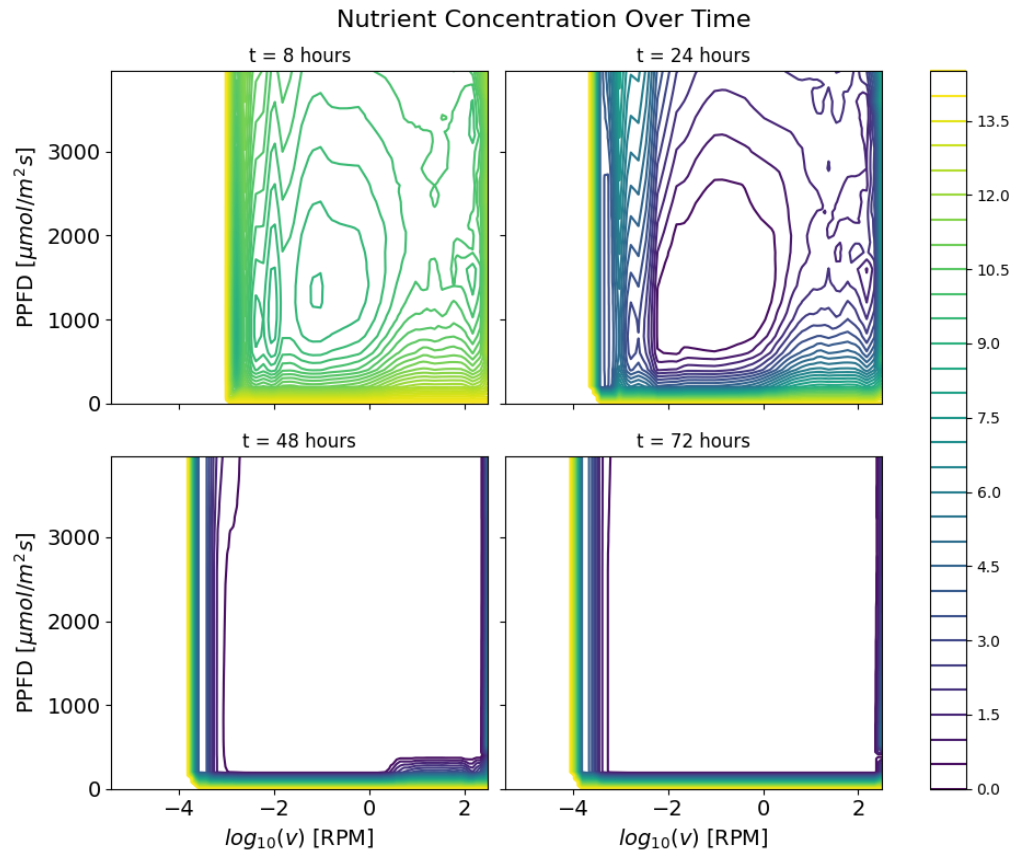


Figure A.9: This figure displays the contour plots to supplement the results in Figure 2.9.